

# Optomechanical self-organization in a mesoscopic atom array

Jacquelyn Ho,<sup>1,2</sup> Yue-Hui Lu,<sup>1,2</sup> Tai Xiang,<sup>1,2</sup> Cosimo C. Rusconi,<sup>3</sup> Stuart J. Masson,<sup>3,4</sup> Ana Asenjo-Garcia,<sup>3</sup> Zhenjie Yan,<sup>1,2</sup> and Dan M. Stamper-Kurn<sup>1,2,5,\*</sup>

<sup>1</sup>*Department of Physics, University of California, Berkeley, California 94720*

<sup>2</sup>*Challenge Institute for Quantum Computation, University of California, Berkeley, California 94720*

<sup>3</sup>*Department of Physics, Columbia University, New York, NY 10027*

<sup>4</sup>*Department of Physics, University of South Florida, Tampa, Florida 33620*

<sup>5</sup>*Materials Sciences Division, Lawrence Berkeley National Laboratory, Berkeley, California 94720*

A fundamental challenge in modern physics is bridging the gap between an exact description of few-body microscopic systems and the emergent description of many-body macroscopic systems. This gap may be bridged by tracing the properties of well-controlled intermediate-size mesoscopic systems. Here, we study mesoscopic signatures of a spatial self-organization phase transition in deterministically prepared arrays of between 10 and 22 atoms inside an optical cavity. Through precise engineering of the atom-cavity interactions, we reveal how critical behavior depends on atom number. We identify characteristic dynamical behaviors related to symmetry breaking and system size in the self-organized regime, and observe a finite optomechanical susceptibility at the critical point. This work opens the door to probing particle-number- and time-resolved properties of phase transitions in mesoscopic systems.

The scale of a physical system plays a key role in determining its material properties. With increasing size comes increasing complexity, and complexity leads to the emergence of macroscopic phenomena that, often, cannot be extrapolated from microscopic behaviors [1]. A well-known example of this paradigm is the appearance of phase transitions in the thermodynamic limit, i.e. as a system's particle number tends to infinity. In between the microscopic and macroscopic extremes lies the mesoscopic regime. Mesoscopic systems not only exhibit characteristics of macroscopic systems, but also host a variety of rich properties themselves. In systems of intermediate size, assumptions of local equilibrium break down and internal microstructures may affect properties on longer length scales [2]. The fact that microscopic fluctuations have a measurable influence on mesoscopic scales also makes mesoscopic systems an interesting playground for the study of critical phenomena and phase transitions. Predicted behaviors of mesoscopic systems near critical points include the smoothing out of the slope of the order parameter [3], finite-size scaling exponents [4], and switching dynamics between symmetry-broken phases [5–7].

Technical advances in engineering, probing and measuring mesoscopic systems have propelled experiments in a variety of physical platforms. Notable examples include solid state systems [8, 9], nanostructured [10] and nanomechanical systems [11–14], nanomagnets [15, 16], and cold atoms and ions [17–23]. Breakthroughs in the control of atoms trapped in optical tweezer arrays represent a leap forward in precisely constructing mesoscopic, ultracold atomic systems. We show that deterministic control over particle number and interaction strength can be achieved with an optical tweezer array inside a standing-wave optical cavity. The unprecedented versatility in the positioning of individual atoms offered by tweezer arrays has enabled numerous advances in quantum simulation, sensing, and information processing [24, 25]. We use the tweezers to adjust the position of each atom with respect to the spatial structure of the cavity field, thereby precisely

programming the atom-cavity coupling strength. This system uniquely lends itself to the detailed study of optomechanics in mesoscopic samples.

We focus on the mechanical self-organization generated by light-mediated forces among optically excited atoms within an optical cavity [26, 27]. When such atoms are driven by coherent light above a certain intensity, they exhibit a phase transition in which they spontaneously scatter light into the cavity. That light creates a spatially dependent potential on the atoms that causes them to self-organize and superradiantly emit into the cavity with a phase that breaks  $\mathbb{Z}_2$  symmetry. This self-organization phase transition maps onto the Dicke model [28, 29]. Previous experiments on the optomechanical Dicke phase transition [29] and other phenomena arising from cavity-mediated forces among atoms [30–34] were conducted on bulk macroscopic samples, with particle numbers  $N \gtrsim 10^5$ . Here, we realize the mesoscopic limit of the Dicke phase transition in deterministically prepared tweezer arrays containing between 10 and 22 atoms. We observe a critical point that depends on atom number, a finite switching time scale between self-organized states, and a collectively altered susceptibility to external forces. This setup allows us to study the crossover from the few- to many-body regime of phase transitions, advancing our knowledge of finite size effects and dynamical behavior in mesoscopic systems.

## CAVITY-MEDIATED INTERACTIONS AND SELF-ORGANIZATION

To realize mesoscopic self-organization, we use the experimental setup schematically shown in Fig. 1A. It contains a one-dimensional tweezer array into which we load a deterministic number  $N$  of  $^{87}\text{Rb}$  atoms. The array is aligned along the axis of a high-finesse Fabry-Pérot optical cavity (the  $z$ -axis). The cavity is placed in-vacuum and has a  $\text{TEM}_{00}$  mode whose frequency,  $\omega_c$ , lies near the resonance frequency,  $\omega_a$ ,

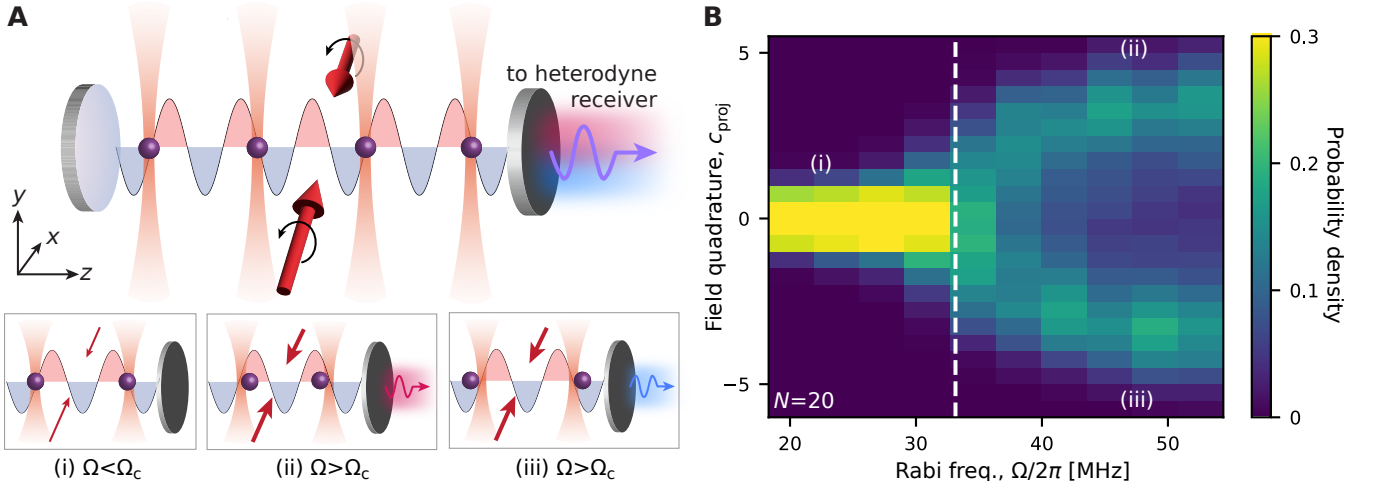


FIG. 1. **Cavity-induced self-organization.** (A) Schematic of the experimental setup. Optically tweezed atoms are placed at the nodes of the cavity field at half-integer wavelength spacing ( $1.5\lambda$  shown in figure for convenience). The atoms are driven by a pair of circularly polarized counter-propagating pump beams. The transmitted cavity field is detected with a heterodyne receiver. Insets (i-iii) illustrate self-organization. (i) At pump strengths below the critical point, the atoms remain centered at the cavity nodes and on average emit zero field. Above the critical point, atoms self-organize by moving toward either the (ii) positive (red) or (iii) negative (blue) antinodes. (B) Probability distributions of cavity field projections from repeated measurements. The results shown are based on data collected with  $N = 20$ ,  $\Delta_{\text{pc}} = -2\pi \times 1.9$  MHz and  $\Delta_{\text{pa}} = -2\pi \times 80$  MHz. The field distributions are plotted for different values of  $\Omega$ . The data are averaged over  $5 \mu\text{s}$  intervals and are sampled from the first  $100 \mu\text{s}$  after the pump ramp-up has finished. The labels (i), (ii), and (iii) correspond to the drawings in (A). The white dashed line indicates the critical point fitted from the data.

of the  $^{87}\text{Rb}$   $F = 2 \rightarrow F' = 3$   $D_2$  transition (wavelength  $\lambda = 780$  nm) [35, 36]. The atoms, prepared in the  $F = 2$  ground state manifold, are exposed to a circularly polarized standing wave pump beam of frequency  $\omega_p$  (detuned from the atoms by  $\Delta_{\text{pa}} = \omega_p - \omega_a$  and from the cavity by  $\Delta_{\text{pc}} = \omega_p - \omega_c$ ) propagating along the  $x$ -axis. The circularly polarized pump creates a fictitious magnetic field along  $x$  through vector light shifts and defines the atomic quantization axis. The pump drives the  $\sigma^-$  electric dipole transition of the atoms and its power is linearly ramped up to the desired value in  $50 \mu\text{s}$ . The initial ramp optically pumps the atoms into the  $|F = 2, m_F = -2\rangle$  stretched state, whence the atoms are excited on the cycling transition, thereby restricting spin dynamics to a two-level system. We achieve a maximal vacuum Rabi coupling of  $g_0 = 2\pi \times 3.1/\sqrt{2}$  MHz between the  $y$ -polarized cavity field and the atomic  $\sigma^-$  transition. The cavity half-linewidth is  $\kappa = 2\pi \times 0.53$  MHz, resulting in a sub- $\mu\text{s}$  cavity response time defined by  $1/\kappa$ . Given that the atomic half-linewidth is  $\gamma = 2\pi \times 3.0$  MHz, we achieve a single-atom cooperativity  $C = g_0^2/(2\kappa\gamma) = 1.5$  [37]. Because the atom-cavity interaction depends strongly on the spatial structure of the pump and cavity standing waves [38–41], the tweezers are aligned to be all within the same pump antinode wavefront (so the atoms all experience the same pump Rabi frequency,  $\Omega$ ) and are positioned at cavity nodes spaced  $4.5\lambda$  apart. By spacing the tweezers by a half-integer number of wavelengths, we eliminate biasing in our system due to center-of-mass drift of the tweezer array with respect to the cavity standing wave.

Light inside the cavity creates a potential energy landscape for the atoms through the exchange of cavity photons [27]. For

atom  $n$  at position  $\hat{z}_n$ , the cavity interaction potential, produced by interference between the pump and cavity fields, is proportional to  $S \sin(k\hat{z}_n)(\hat{c} + \hat{c}^\dagger)$ , where  $\hat{c}$  ( $\hat{c}^\dagger$ ) is the bosonic annihilation (creation) operator for a cavity photon,  $S \simeq \Omega g_0/(2\Delta_{\text{pa}})$  is the coherent scattering rate of a pump photon into the cavity, and  $k = 2\pi/\lambda$ . The strength of the potential thus depends on the atom's position inside the cavity and on the magnitude of the cavity field. When the pump is sufficiently detuned from the atomic transition and red-detuned from cavity resonance, the cavity field follows the atomic motion such that  $\hat{c} + \hat{c}^\dagger \propto -S \sum_{m=1}^N \sin(k\hat{z}_m)$ . In this adiabatic regime, the effective potential is minimized when  $\langle \sin(k\hat{z}_n) \rangle = \pm 1$  for all  $n$ . That is, the most favorable configurations of the system are the ones where the atoms self-organize by collectively moving to cavity-field antinodes with the same sign.

The steady state of the optomechanical system is governed by competition between the cavity-mediated interaction and the tweezer potential, which, for tweezers centered at the cavity nodes, is minimized when  $\langle \sin(kz_n) \rangle = 0$  for all  $n$ . This competition gives rise to the emergence of self-organization as a function of  $S$ , which we tune through  $\Omega$ , thus defining a critical pump strength  $\Omega_c$ . For  $\Omega < \Omega_c$ , the tweezers dominate over the cavity field and the atoms remain centered at the cavity nodes (as shown in Fig. 1A(i)). Although the atom array is uncoupled to the cavity when positioned exactly at the nodes, zero-point and thermal fluctuations shift the atom positions, causing the array to emit light incoherently into the cavity. For  $\Omega > \Omega_c$ , the negative curvature of the cavity potential overcomes the positive tweezer trap curvature and it becomes

energetically favorable for all atoms to move towards antinodes with the same sign and for their emission to interfere constructively. The superradiant field's phase is determined by the sign of the antinodes chosen by the atoms (Fig. 1A(ii-iii)). For atoms spaced by a half-integer number of wavelengths, adjacent atoms move in opposite directions to achieve self-organization (antiphase motion), in contrast to integer spacing where the atoms move in the same direction (center-of-mass motion). We refer to the collective mode that is linearly coupled to the cavity as the dominant mode.

To confirm the self-organization experimentally, we detect the cavity field  $\hat{c}$  and observe  $\mathbb{Z}_2$  symmetry breaking. Assuming  $\Delta_{\text{pa}} < 0$  (the case for all data shown), light scattered by the atoms affects one quadrature of the cavity field,  $c_{\text{proj}} = \text{Re}(\langle \hat{c} \rangle) \cos \theta + \text{Im}(\langle \hat{c} \rangle) \sin \theta$ , where  $\theta = \arctan(-\kappa/\langle \tilde{\Delta}_{\text{pc}} \rangle)$ , defined with respect to the phase of the pump field. One finds

$$c_{\text{proj}} = \frac{N\Omega g_0}{2|\Delta_{\text{pa}}|} \left\langle \frac{\hat{\Theta}}{\sqrt{\tilde{\Delta}_{\text{pc}}^2 + \kappa^2}} \right\rangle. \quad (1)$$

We define  $\tilde{\Delta}_{\text{pc}} = \Delta_{\text{pc}} - \sum_{n=1}^N g_0^2 \sin^2(k\hat{z}_n)/\Delta_{\text{pa}}$  as the effective cavity detuning including the dispersive shift from the atoms. The cavity field is proportional to the operator

$$\hat{\Theta} \equiv \frac{1}{N} \sum_{n=1}^N \sin(k\hat{z}_n), \quad (2)$$

whose mean value can be interpreted as the order parameter. For atoms trapped at the nodes  $\langle \hat{\Theta} \rangle = 0$ , while for atoms at the antinodes  $\langle \hat{\Theta} \rangle = \pm 1$ . Thus  $\langle \hat{\Theta} \rangle$  takes the role of an effective magnetization for the system [26, 42].

To detect the complex cavity field  $\hat{c}$ , we send  $y$ -polarized emission from one cavity mirror to a heterodyne receiver (see fig. S1) and record the signal for a total time of 250  $\mu\text{s}$ , including the 50  $\mu\text{s}$  pump ramp-up time. We filter the time trace with an adjustable averaging time, ranging from 5  $\mu\text{s}$  to 50  $\mu\text{s}$ ; we average for a minimum of 5  $\mu\text{s}$  because increased noise at shorter averaging times compromises the signal-to-noise ratio of the extracted cavity field. The values obtained at each step of the filter are treated as individual data points for  $\hat{c}$ . We determine the angle  $\theta$  by referencing the phase of the distribution of  $\hat{c}$  to that obtained with all atoms placed at antinodes of the same sign. We then project each value of  $\hat{c}$  onto the axis defined by  $\theta$  to obtain  $c_{\text{proj}}$  (see materials and methods and fig. S2). Our measured  $c_{\text{proj}}$  is scaled such that  $c_{\text{proj}}^2$  is the average photon number in the cavity.

To observe bifurcation in the distributions of  $c_{\text{proj}}$ , we repeat the measurement many times at different pump strengths and analyze the heterodyne data from  $t = 0$  to  $t = 100 \mu\text{s}$  (where  $t = 0$  is the end of the pump ramp-up) using a 5  $\mu\text{s}$  averaging time. Due to heating of the atoms from continuous exposure to pump light [43, 44], we constrain this analysis to the 100  $\mu\text{s}$  span described above. The distributions of  $c_{\text{proj}}$  show a striking bifurcation as the pump strength is increased.

An example is shown in Fig. 1B. We see that once  $\Omega$  surpasses a threshold near  $2\pi \times 30$  MHz, the single peak at  $c_{\text{proj}} = 0$  splits into two symmetric branches with finite field amplitude.

The simplest model that captures this physics is purely mechanical and lossless, with an effective Hamiltonian

$$\hat{H}_{\text{eff}} \equiv \sum_{n=1}^N \left[ \frac{\hat{p}_n^2}{2M} + \frac{M}{2} \nu^2 (\hat{z}_n - z_{0n})^2 \right] + \hbar \mathcal{D} N^2 \hat{\Theta}^2. \quad (3)$$

Here,  $M$  is the atomic mass of  $^{87}\text{Rb}$ ,  $\nu = 2\pi \times 93$  kHz is the tweezer trap frequency (in the harmonic approximation),  $\hbar$  is the reduced Planck constant, and  $\mathcal{D} \equiv \left( \frac{g_0 \Omega}{2\Delta_{\text{pa}}} \right)^2 \tilde{\Delta}_{\text{pc}} / (\tilde{\Delta}_{\text{pc}}^2 + \kappa^2)$  is the strength of the cavity-induced mechanical potential, whose sign depends on  $\tilde{\Delta}_{\text{pc}}$ . The tweezer positions are  $z_{0n} = 4.5\lambda \times n$ .

However, thermal fluctuations as well as motion of the atoms perpendicular to the cavity axis are relevant for a quantitative description of the experiment. By means of a more refined optomechanical model [45], the critical pump strength is found to be

$$\Omega_c(T) = \sqrt{\frac{2M\nu^2 \Delta_{\text{pa}}^2 (\Delta_{\text{pc}}^2(T) + \kappa^2)}{N g_0^2 k^2 |\Delta_{\text{pc}}(T)| \hbar \varepsilon(T)}}, \quad (4)$$

where  $T$  is the atomic motional temperature and the temperature-dependent factor  $\varepsilon(T)$  is defined in the supplementary text. The dependencies of  $\Omega_c$  on  $N$  and  $\Delta_{\text{pa}}$  are studied in this work (see Fig. 2 and fig. S4). Equation (4) includes two different thermal effects on the critical pump strength. First, taking an average over the thermal motional shift of the atoms yields a net shift of the cavity resonance  $\Delta_{\text{pc}}(T) \equiv \langle \tilde{\Delta}_{\text{pc}} \rangle$ . Second, thermal fluctuations allow the atoms to probe the non-linearity of the effective mechanical potential in  $\hat{\Theta}^2$ . This leads to an increase in the critical pump strength proportional to the factor  $1/\varepsilon(T)$  in Equation (4). Using a temperature of  $35 \pm 10 \mu\text{K}$ , determined from an independent measurement [38], Equation (4) predicts  $\Omega_c = 2\pi \times (26.5 \pm 2.5)$  MHz for the parameter settings in Fig. 1B.

To determine  $\Omega_c$  quantitatively from the data, we draw inspiration from Landau's theory of phase transitions [46]. If we only consider the contribution of the dominant mode to the Hamiltonian in Equation (3), the potential energy becomes  $\frac{1}{2} N M \nu^2 \hat{z}_{\text{dom}}^2 + \hbar \mathcal{D} N^2 \sin^2(k\hat{z}_{\text{dom}})$ , where  $\hat{z}_{\text{dom}}$  is the displacement of the dominant mode with respect to the cavity nodes. If we consider the distribution of positions to be a Boltzmann distribution determined by the local potential energy, and expand the potential energy to fourth order in  $\hat{z}_{\text{dom}}$ , we obtain a probability distribution  $p(z_{\text{dom}})$  of the form

$$p(z_{\text{dom}}) \propto \exp(-B z_{\text{dom}}^2 - D z_{\text{dom}}^4), \quad (5)$$

where  $B$  and  $D$  are parameter-dependent constants and  $z_{\text{dom}} \equiv \langle \hat{z}_{\text{dom}} \rangle$ . According to Landau's theory, a second order phase transition occurs at  $B = 0$ . Because  $c_{\text{proj}}$  is proportional to  $z_{\text{dom}}$  to leading order, we fit the observed distributions of  $c_{\text{proj}}$  to Equation (5) and extract the coefficient  $B$

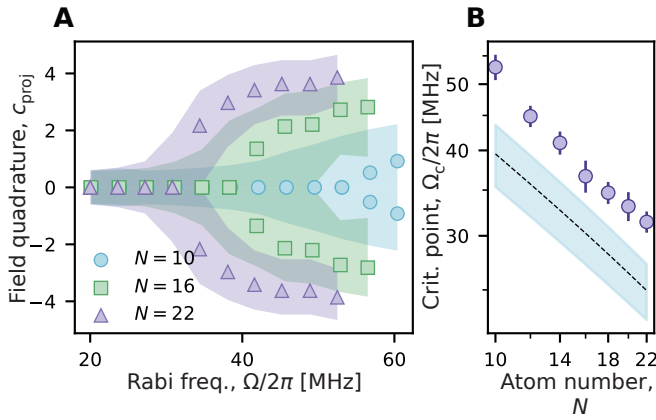


FIG. 2. **Dependence of the critical point on atom number.** (A) Bifurcation data for  $N = 10$  (circles),  $N = 16$  (squares), and  $N = 22$  (triangles). Shaded areas show the width of the distribution at half maximum while markers show the maxima of the fitted Boltzmann distribution. (B) Experimentally measured  $\Omega_c$  (circles) for different  $N$  plotted on a logarithmic scale and the theoretical prediction of Equation (4), based on an independent temperature measurement of  $T = 35 \pm 10 \mu\text{K}$  (black dashed line and light blue shaded area). Error bars represent statistical errors from fits of the parameter  $B$  and drift of the pump power over the course of the experiment, estimated to be 10%. The reported values of  $\Omega_c$  account for systematic errors due to Gaussian detector noise and the Gaussian intensity profile of the pump beam. We note that there is an additional systematic error of +6.0% and -8.5% on our calibration of  $\Omega$  (see supplementary text for details). All data in figure are taken at  $\Delta_{\text{pa}} = -2\pi \times 80 \text{ MHz}$  and  $\Delta_{\text{pc}} = -2\pi \times 1.9 \text{ MHz}$ .

to determine where  $\Omega_c$  occurs. Analyzing the distributions of  $c_{\text{proj}}$ , we observe that the fits to the Boltzmann distribution match the data well (see fig. S5 and supplementary text) even though the system is driven and dissipative. From the data in Fig. 1B, we extract an experimental  $\Omega_c = 2\pi \times (33.1_{-2.8}^{+2.0} \text{stat} \pm 1.6_{\text{stat}}) \text{ MHz}$ . This measurement is slightly above the prediction of Equation (4) for our independent measurement of the initial temperature of the trapped atoms. The slight discrepancy may be caused by heating of the trapped atoms during the experiment, owing to light scattering. Nonetheless, when statistical and systematic errors (primarily resulting from uncertainty in our calibration of  $\Omega$  [45]) are taken into consideration, the measurement falls within the error of the prediction of Equation (4) for our independent temperature measurement.

### MESOSCOPIC SIGNATURES OF A PHASE TRANSITION

To probe the evolution of system properties with size directly, we examine how critical behavior varies with atom number. We first examine the dependence of  $\Omega_c$  on  $N$ , and find that  $\Omega_c$  diminishes as  $N$  increases. Quantitatively, for an averaging time of  $5 \mu\text{s}$ , we almost recover the  $\sim 1/\sqrt{N}$  dependence predicted by Equation (4), shown in Fig. 2B. Though the critical point's scaling with  $N$  has been measured

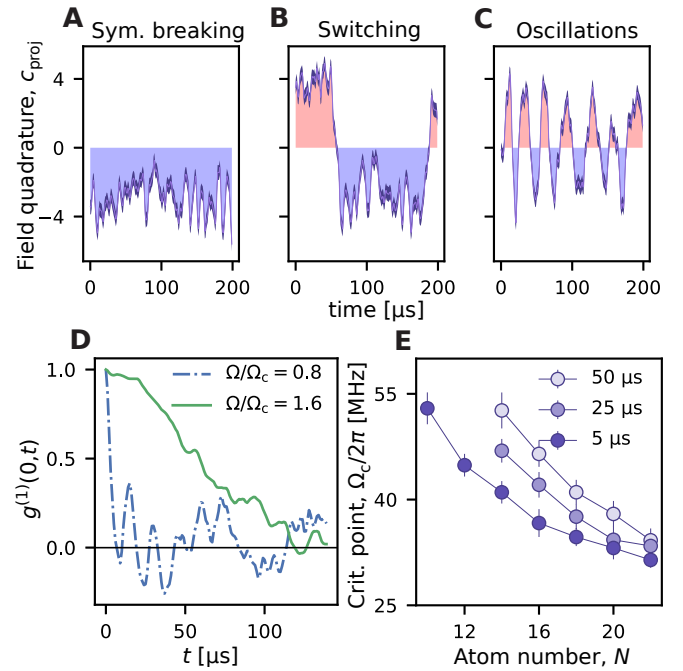


FIG. 3. **Lifetime of the self-organized state.** Above the critical point, we observe three dynamical behaviors in the cavity field time traces: (A) symmetry breaking, (B) switching, and (C) rapid oscillations. Time is measured from the end of the pump ramp-up. Shaded areas show the time spent in the  $c_{\text{proj}} > 0$  state (red) and the  $c_{\text{proj}} < 0$  state (blue). Shaded purple regions indicate the shot noise level. Data are shown for  $N = 20$ ,  $\Omega = 2\pi \times 45.4 \text{ MHz}$ . (D)  $g^{(1)}(0, t)$  for  $N = 20$  at  $\Omega < \Omega_c$  and  $\Omega > \Omega_c$ . When the system is self-organized,  $g^{(1)}(0, t)$  decays on a much longer timescale. All data in figure are taken at  $\Delta_{\text{pa}} = -2\pi \times 80 \text{ MHz}$  and  $\Delta_{\text{pc}} = -2\pi \times 1.9 \text{ MHz}$ . (E) Dependence of the critical point on  $N$  for different averaging times. At larger  $N$ , the curves converge, indicating that self-organization persists on longer timescales. At lower  $N$ , the separation between the curves grows due to the transience of the mesoscopic system. The measurements at  $25 \mu\text{s}$  and  $50 \mu\text{s}$  for  $N < 14$  are absent because the transition was not reached in the range of  $\Omega$  values scanned. The plotted  $\Omega_c$  data are subject to the same systematic errors as described in Fig. 2B. Lines are guides to the eye.

before in macroscopic bosonic and fermionic realizations of the superradiant phase transition [43, 47], our work shows that the  $N$ -dependence is also observable in a regime far from the thermodynamic limit. In Fig. 2B, the data appear above the prediction of Equation (4) if we use the temperature from our independent measurement, implying that the atoms have been heated to a temperature close to  $66 \mu\text{K}$  at the time of observation.

Atomic self-organization in a cavity can be compared with the crossover between a magnetized and unmagnetized state in a spin system. Notably, due to the infinite-range character of the interaction, the crossover does not occur by forming domains of increasing size as the critical coupling  $\Omega_c$  is approached [42]. Instead, the behavior of  $\langle \hat{\Theta} \rangle$  above the transition is analogous to that of a superparamagnet: As discussed in seminal work by Néel [48], small ferromagnetic particles are

subject to thermal fluctuations that cause their magnetization to relax on a time scale that grows with the particle volume. Averaging the magnetization over times much longer than the relaxation time results in zero net magnetization, while averaging over times much shorter than the relaxation time allows for observation of quasistatic magnetic ordering [5]. We similarly find that mesoscopic self-organization of atoms has a characteristic lifetime that depends on system size.

To reveal the dynamics of the magnetization order parameter  $\langle \hat{\Theta} \rangle$ , we take advantage of the cavity's  $\mu\text{s}$ -scale readout capability [35]. In Fig. 3, we examine single-shot time traces of  $c_{\text{proj}}$ , time correlations of the field, as well as the  $N$ -dependence of the critical point as we increase the averaging time. Fig. 3A-C show single-shot time traces representative of observed dynamical behaviors in the self-organized regime: symmetry breaking, switching, and rapid oscillations. For a macroscopic atom number, only symmetry breaking should occur, while for a mesoscopic atom number, fluctuations away from equilibrium can lead to switching between stable states of the system [42]. The rapid oscillation events are rare, occurring in only 2 out of the 180 shots obtained at the shown parameter setting; we expect they result from the energy in the dominant mode being above the energy gap separating the two symmetry-broken states.

To highlight the difference in dynamical behavior below and above the critical point, we calculate the first-order coherence function of the field quadrature  $g^{(1)}(t_1, t_2)$ , defined as  $g^{(1)}(t_1, t_2) = \langle c_{\text{proj}}^*(t_1)c_{\text{proj}}(t_2) \rangle / \sqrt{\langle |c_{\text{proj}}(t_1)|^2 \rangle \langle |c_{\text{proj}}(t_2)|^2 \rangle}$ , where the angle brackets denote averaging over multiple shots. In particular,  $g^{(1)}(0, t)$  indicates how correlated the field at time  $t_2 = t$  is to the field at time  $t_1 = 0$ , where  $t_1 = 0$  is chosen to be at the end of the pump ramp-up. Symmetry breaking is indicated by  $g^{(1)}(0, t)$  remaining high for extended  $t$ . In Fig. 3D, we see that when  $\Omega/\Omega_c = 0.8$ ,  $g^{(1)}(0, t)$  decays rapidly, indicating the absence of symmetry breaking, and exhibits oscillations at approximately 60 kHz, corresponding to the softened trap frequency. At  $\Omega/\Omega_c = 1.6$ ,  $g^{(1)}(0, t)$  decays on a much longer timescale and oscillations are absent, indicating a prolonged lifetime of the symmetry-broken states.

We next observe the  $N$ -dependence of the lifetime of the self-organized state. As discussed above, the characteristic behavior of the system depends on the time over which  $\langle \hat{\Theta} \rangle$  is averaged. On short time scales, the system displays signatures of symmetry breaking, while on long time scales, the system switches between the two stable states. As a result, in Fig. 3E, we see that the nominal  $\Omega_c$  increases as we increase the averaging time from 5 to 50  $\mu\text{s}$ . Remarkably, we see that  $\Omega_c$  increases significantly at lower  $N$  but less so at higher  $N$ . This indicates that as the system size decreases, the characteristic time scale over which the system remains self-organized also decreases. We thus observe a key feature of this mesoscopic system: Averaging  $\langle \hat{\Theta} \rangle$  over times longer than the  $N$ -dependent lifetime erases signatures of symmetry breaking.

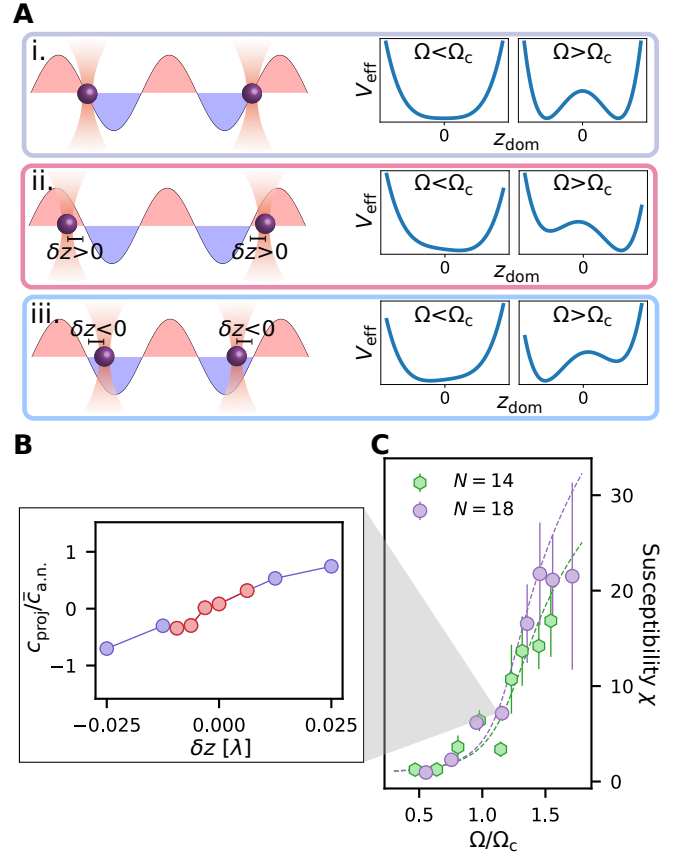


FIG. 4. **Optomechanical susceptibility.** (A) Schematic of the susceptibility measurement. The dominant mode of the array ( $z_{\text{dom}}$ ) is displaced by  $\delta z$ . When  $\delta z = 0$ , the effective potential  $V_{\text{eff}}$  on the atoms is symmetric about  $z_{\text{dom}} = 0$  (i). For  $|\delta z| > 0$ ,  $V_{\text{eff}}$  tilts in the direction of the bias (ii-iii). (B) Distributions of  $c_{\text{proj}}/\bar{c}_{\text{a.n.}}$  and their mean values (circles) at various  $\delta z$  for  $N = 18$ ,  $\Omega/\Omega_c = 1.16$ . Measurement of  $\partial(\bar{c}_{\text{proj}}/\bar{c}_{\text{a.n.}})/\partial(\delta z)|_{\delta z=0}$  is taken by fitting the slope of  $\bar{c}_{\text{proj}}/\bar{c}_{\text{a.n.}}$  for  $-0.01\lambda \leq \delta z \leq 0.01\lambda$  (red circles). (C) Susceptibility  $\chi$  at various  $\Omega/\Omega_c$  for  $N = 14$  and  $N = 18$ . The data (hexagons and circles) are plotted together with the theoretical prediction based on the Boltzmann distribution (dashed lines). All data in figure are taken at  $\Delta_{\text{pa}} = -2\pi \times 80$  MHz and  $\Delta_{\text{pc}} = -2\pi \times 1.9$  MHz.

### FINITE SUSCEPTIBILITY AT CRITICALITY

The positional control afforded by the tweezers not only allows us to observe spontaneous symmetry breaking, but also to explicitly break symmetry with nanometer-scale precision and probe the system's response. By displacing adjacent tweezers in opposite directions by an amount  $\delta z$ , we introduce a constant force proportional to  $\delta z$  on the atoms that biases the dominant mode (Fig. 4A). Generally, the amount a system moves in response to an applied force is characterized by its mechanical susceptibility. In our case,  $c_{\text{proj}}$  serves as a proxy for the atom positions. As such, we obtain the optomechanical

susceptibility,  $\chi$ , which we define as

$$\chi \equiv \frac{1}{k\bar{c}_{\text{a.n.}}} \left. \frac{\partial \bar{c}_{\text{proj}}}{\partial(\delta z)} \right|_{\delta z=0}. \quad (6)$$

Here,  $\bar{c}_{\text{a.n.}}$  is the measurement of  $\bar{c}_{\text{proj}}$  when the tweezers are positioned at the positive antinodes. The overbar indicates an average over the distribution of  $c_{\text{proj}}$  obtained from the first 50  $\mu\text{s}$  of multiple shots. The quantity  $\partial(\bar{c}_{\text{proj}}/\bar{c}_{\text{a.n.}})/\partial(\delta z)|_{\delta z=0}$  is measured by fitting the slope of  $\bar{c}_{\text{proj}}/\bar{c}_{\text{a.n.}}$  in the range  $-0.01\lambda \leq \delta z \leq 0.01\lambda$  for  $N = 18$  (red circles in Fig. 4B) and  $N = 14$ . We note that the atoms are initialized with root-mean-square thermal fluctuations in position of about 100 nm, leading to a thermal Lamb-Dicke parameter of about 0.8 [45].

From measurement of  $\chi$  for  $N = 14$  and  $N = 18$  at different values of  $\Omega/\Omega_c$  (Fig. 4C), we make two observations: 1) while  $\chi$  increases with  $\Omega/\Omega_c$ , it does not diverge at the critical point as one would expect for a second-order phase transition in a macroscopic system, and 2) the value of  $\chi$  grows with atom number for  $\Omega/\Omega_c > 1$ . These observations can be explained by a model assuming  $\chi \simeq \partial\langle z_{\text{dom}} \rangle / \partial(\delta z)|_{\delta z=0} = NM\nu^2 \langle \Delta z_{\text{dom}}^2 \rangle / (k_B T)|_{\delta z=0}$ , where angle brackets indicate a thermal average including the tweezer bias  $\delta z$  [45]. Thus, the susceptibility is directly related to the size of fluctuations in the system through the variance  $\langle \Delta z_{\text{dom}}^2 \rangle$ . In a macroscopic system, one would expect  $\chi$  to diverge according to  $1/(1 - (\Omega/\Omega_c)^2)$  as  $\Omega$  approaches  $\Omega_c$ . Instead, because of our finite atom number, our model predicts that  $\chi$  should remain finite at the critical point.

Specifically, at the critical point, our model predicts that  $\chi$  should be approximately proportional to  $\sqrt{N}$  as a result of the variance  $\langle \Delta z_{\text{dom}}^2 \rangle$  scaling as  $1/\sqrt{N}$  at leading order. This has a simple interpretation: At smaller  $N$ , the fluctuations in  $z_{\text{dom}}$  are larger and the atoms sample the quartic part of the effective optomechanical potential  $V_{\text{eff}}$ , which provides the confinement that prevents the susceptibility from diverging. While we observe finite  $\chi$  at the critical point, we are unable to resolve the  $\sqrt{N}$ -dependence due to the quality of our data. Nonetheless, we emphasize that this observation of finite  $\chi$  is a direct measure of mesoscopic fluctuations and not just a result of non-zero temperature—a macroscopic system at non-zero temperature would still exhibit a diverging susceptibility. As  $\Omega/\Omega_c$  is increased beyond 1, our model predicts that  $\chi$  should continue to grow and eventually scale proportionally to  $N$ , before saturating at a value of  $NM\nu^2\lambda^2/(16k_B T)$ . For  $\Omega \gg \Omega_c$ , the  $\delta z$  required to confine  $\langle z_{\text{dom}} \rangle$  effectively to one of the minima of  $V_{\text{eff}}$  scales inversely with  $N$ , leading to  $\chi \propto N$ . We note that  $\chi$  continuing to increase for  $\Omega > \Omega_c$  is a consequence of us applying the tweezer shift  $\delta z$  to break symmetry before the cavity interaction is turned on, analogous to applying a magnetic field to a spin system before lowering its temperature below the Curie point. In contrast, if the tweezer shift were applied after the cavity interaction, one might expect  $\chi$  to peak at  $\Omega = \Omega_c$ . Accordingly, we see the separation between the  $N = 14$  and  $N = 18$  data become more pronounced as we increase  $\Omega$  beyond  $\Omega_c$ , consistent with the pre-

diction of  $\chi$  approaching linear scaling with  $N$ . These results highlight how the response of mesoscopic systems deviates from that of macroscopic systems.

## DISCUSSION AND OUTLOOK

We have studied self-organization, bifurcation, and symmetry breaking as well as mesoscopic dynamics and response due to light-mediated interactions in an atom array. The deterministic atom number and precise control over interactions necessary for this work were achieved by interfacing an optical tweezer array with an optical cavity, opening new directions for these systems. The realization of mesoscopic self-organization with control over individual atoms has significant implications not just for our fundamental understanding of mesoscopic systems, but also for quantum simulation, optimization, and metrology. On one hand, the dynamics of the cavity field provide a plethora of information that may further our understanding of nonequilibrium physics in mesoscopic systems [49] and pave the way for time-resolved quantum simulation [50, 51]. On the other hand, mesoscopic self-organization may also open the door to programmable engineering [52] of exotic symmetry-breaking phases of matter [53], for instance by illuminating groups of atoms with different phases of pump light. This system can also be used to implement a quantum numerical solver for a variety of classically hard computational problems [54–56], where the tweezer array allows for highly programmable initial conditions. Additionally, the optomechanical susceptibility near the critical point can be a resource for enhanced sensing of applied forces [57–59].

## ACKNOWLEDGMENTS

We thank Nathan Song for assistance in the lab.

**Funding:** We acknowledge support from the AFOSR (Grant No. FA9550-1910328 and Young Investigator Prize Grant No. 21RT0751), from ARO through the MURI program (Grant No. W911NF-20-1-0136), from DARPA (Grant No. W911NF2010090), from the NSF (QLCI program through grant number OMA-2016245, and CAREER Award No. 2047380), from the David and Lucile Packard Foundation, and from the U.S. Department of Energy, Office of Science, National Quantum Information Science Research Centers, Quantum Systems Accelerator. J.H. acknowledges support from the Department of Defense through the National Defense Science and Engineering Graduate (NDSEG) Fellowship Program. C.C.R. acknowledges support from the European Union’s Horizon Europe program under the Marie Skłodowska Curie Action LIME (Grant No. 101105916).

**Author contributions:** J.H., Y.-H.L., Z.Y., and T.X. contributed to building the experimental setup, performing the experiments, and analyzing the data. C.C.R., S.J.M., A.A.-G., D.M.S.-K., and J.H. contributed to the theoretical model. Z.Y.

and D.M.S.-K. conceived the experiments. All authors contributed to writing of the manuscript and discussed the results. All work was supervised by D.M.S.-K. and A.A.-G.

**Competing interests:** The authors declare no competing interests.

**Data and materials availability:** Data are available from the corresponding author upon reasonable request.

---

\* [dmsk@berkeley.edu](mailto:dmsk@berkeley.edu)

- [1] P. Anderson, More Is Different, *Science* **177**, 393 (1972).
- [2] D. Jou and L. Restuccia, Mesoscopic transport equations and contemporary thermodynamics: An introduction, *Contemporary Physics* **52**, 465 (2011).
- [3] F. Iachello and N. V. Zamfir, Quantum Phase Transitions in Mesoscopic Systems, *Physical Review Letters* **92**, 212501 (2004).
- [4] J. Vidal and S. Dusuel, Finite-size scaling exponents in the Dicke model, *Europhysics Letters (EPL)* **74**, 817 (2006).
- [5] M. Knobel, W. C. Nunes, L. M. Socolovsky, E. De Biasi, J. M. Vargas, and J. C. Denardin, Superparamagnetism and Other Magnetic Features in Granular Materials: A Review on Ideal and Real Systems, *Journal of Nanoscience and Nanotechnology* **8**, 2836 (2008).
- [6] K. C. Stitely, S. J. Masson, A. Giraldo, B. Krauskopf, and S. Parkins, Superradiant switching, quantum hysteresis, and oscillations in a generalized Dicke model, *Physical Review A* **102**, 063702 (2020).
- [7] S. D. Slöetjes, B. Hjörvarsson, and V. Kapaklis, The effect of confinement on thermal fluctuations in nanomagnets, *Applied Physics Letters* **118**, 142407 (2021).
- [8] G. Karapetrov, J. Fedor, M. Iavarone, D. Rosenmann, and W. K. Kwok, Direct Observation of Geometrical Phase Transitions in Mesoscopic Superconductors by Scanning Tunneling Microscopy, *Physical Review Letters* **95**, 167002 (2005).
- [9] J. Bird, K. Ishibashi, Y. Aoyagi, T. Sugano, R. Akis, D. Ferry, D. Pivin, K. Connolly, R. Taylor, R. Newbury, D. Olatona, A. Micolich, R. Wirtz, Y. Ochiai, and Y. Okubo, Quantum transport in open mesoscopic cavities, *Chaos, Solitons & Fractals* **8**, 1299 (1997).
- [10] A. Knoll, K. S. Lyakhova, A. Horvat, G. Krausch, G. J. A. Sevink, A. V. Zvelindovsky, and R. Magerle, Direct imaging and mesoscale modelling of phase transitions in a nanostructured fluid, *Nature Materials* **3**, 886 (2004).
- [11] M. H. Matheny, J. Emenheiser, W. Fon, A. Chapman, A. Salova, M. Rohden, J. Li, M. Hudoba De Badyn, M. Pósfai, L. Duenas-Osorio, M. Mesbahi, J. P. Crutchfield, M. C. Cross, R. M. D'Souza, and M. L. Roukes, Exotic states in a simple network of nanoelectromechanical oscillators, *Science* **363**, eaav7932 (2019).
- [12] E. A. Wollack, A. Y. Cleland, R. G. Gruenke, Z. Wang, P. Arrangoiz-Arriola, and A. H. Safavi-Naeini, Quantum state preparation and tomography of entangled mechanical resonators, *Nature* **604**, 463 (2022).
- [13] M. Mirhosseini, A. Sipahigil, M. Kalaei, and O. Painter, Superconducting qubit to optical photon transduction, *Nature* **588**, 599 (2020).
- [14] H. Ren, T. Shah, H. Pfeifer, C. Brendel, V. Peano, F. Marquardt, and O. Painter, Topological phonon transport in an optomechanical system, *Nature Communications* **13**, 3476 (2022).
- [15] L. H. F. Andrade, A. Laraoui, M. Vomir, D. Muller, J.-P. Stoquert, C. Estournès, E. Beaurepaire, and J.-Y. Bigot, Damped Precession of the Magnetization Vector of Superparamagnetic Nanoparticles Excited by Femtosecond Optical Pulses, *Physical Review Letters* **97**, 127401 (2006).
- [16] C. Thirion, W. Wernsdorfer, and D. Mailly, Switching of magnetization by nonlinear resonance studied in single nanoparticles, *Nature Materials* **2**, 524 (2003).
- [17] L. Bayha, M. Holten, R. Klemt, K. Subramanian, J. Bjerlin, S. M. Reimann, G. M. Bruun, P. M. Preiss, and S. Jochim, Observing the emergence of a quantum phase transition shell by shell, *Nature* **587**, 583 (2020).
- [18] J.-P. Brantut, J. Meineke, D. Stadler, S. Krinner, and T. Esslinger, Conduction of Ultracold Fermions Through a Mesoscopic Channel, *Science* **337**, 1069 (2012).
- [19] J. Zeiher, J. Wolf, J. A. Isaacs, J. Kohler, and D. M. Stamper-Kurn, Tracking Evaporative Cooling of a Mesoscopic Atomic Quantum Gas in Real Time, *Physical Review X* **11**, 041017 (2021).
- [20] D. J. Gorman, B. Hemmerling, E. Megidish, S. A. Moeller, P. Schindler, M. Sarovar, and H. Haeflner, Engineering Vibrationally Assisted Energy Transfer in a Trapped-Ion Quantum Simulator, *Physical Review X* **8**, 011038 (2018).
- [21] Y. Guo, H. Yao, S. Ramanjanappa, S. Dhar, M. Horvath, L. Pizzino, T. Giamarchi, M. Landini, and H.-C. Nägerl, Observation of the 2D–1D crossover in strongly interacting ultracold bosons, *Nature Physics* **20**, 934 (2024).
- [22] A. Safavi-Naini, R. J. Lewis-Swan, J. G. Bohnet, M. Gärttner, K. A. Gilmore, J. E. Jordan, J. Cohn, J. K. Freericks, A. M. Rey, and J. J. Bollinger, Verification of a Many-Ion Simulator of the Dicke Model Through Slow Quenches across a Phase Transition, *Physical Review Letters* **121**, 040503 (2018).
- [23] A. M. Kaufman, M. E. Tai, A. Lukin, M. Rispoli, R. Schittko, P. M. Preiss, and M. Greiner, Quantum thermalization through entanglement in an isolated many-body system, *Science* **353**, 794 (2016).
- [24] A. M. Kaufman and K.-K. Ni, Quantum science with optical tweezer arrays of ultracold atoms and molecules, *Nature Physics* **17**, 1324 (2021).
- [25] A. Browaeys and T. Lahaye, Many-body physics with individually controlled Rydberg atoms, *Nature Physics* **16**, 132 (2020).
- [26] H. Ritsch, P. Domokos, F. Brennecke, and T. Esslinger, Cold atoms in cavity-generated dynamical optical potentials, *Reviews of Modern Physics* **85**, 553 (2013).
- [27] F. Mivehvar, F. Piazza, T. Donner, and H. Ritsch, Cavity QED with quantum gases: New paradigms in many-body physics, *Advances in Physics* **70**, 1 (2021).
- [28] P. Kirton, M. M. Roses, J. Keeling, and E. G. Dalla Torre, Introduction to the Dicke Model: From Equilibrium to Nonequilibrium, and *Vice Versa*, *Advanced Quantum Technologies* **2**, 1800043 (2019).
- [29] K. Baumann, C. Guerlin, F. Brennecke, and T. Esslinger, Dicke quantum phase transition with a superfluid gas in an optical cavity, *Nature* **464**, 1301 (2010).
- [30] J. Léonard, A. Morales, P. Zupancic, T. Esslinger, and T. Donner, Supersolid formation in a quantum gas breaking a continuous translational symmetry, *Nature* **543**, 87 (2017).
- [31] A. Morales, P. Zupancic, J. Léonard, T. Esslinger, and T. Donner, Coupling two order parameters in a quantum gas, *Nature Materials* **17**, 686 (2018).
- [32] P. Kongkhambut, J. Skulte, L. Mathey, J. G. Cosme, A. Hemmerich, and H. Keßler, Observation of a continuous time crystal, *Science* **377**, 670 (2022).
- [33] Z. Zhiqiang, C. H. Lee, R. Kumar, K. J. Arnold, S. J. Masson,

- A. S. Parkins, and M. D. Barrett, Nonequilibrium phase transition in a spin-1 Dicke model, *Optica* **4**, 424 (2017).
- [34] A. T. Black, H. W. Chan, and V. Vuletić, Observation of Collective Friction Forces due to Spatial Self-Organization of Atoms: From Rayleigh to Bragg Scattering, *Physical Review Letters* **91**, 203001 (2003).
- [35] E. Deist, Y.-H. Lu, J. Ho, M. K. Pasha, J. Zeiher, Z. Yan, and D. M. Stamper-Kurn, Mid-Circuit Cavity Measurement in a Neutral Atom Array, *Physical Review Letters* **129**, 203602 (2022).
- [36] E. Deist, J. A. Gerber, Y.-H. Lu, J. Zeiher, and D. M. Stamper-Kurn, Superresolution Microscopy of Optical Fields Using Tweezer-Trapped Single Atoms, *Physical Review Letters* **128**, 083201 (2022).
- [37] H. J. Kimble, Strong Interactions of Single Atoms and Photons in CavityQED, *Physica Scripta* **T76**, 127 (1998).
- [38] Z. Yan, J. Ho, Y.-H. Lu, S. J. Masson, A. Asenjo-Garcia, and D. M. Stamper-Kurn, Superradiant and Subradiant Cavity Scattering by Atom Arrays, *Physical Review Letters* **131**, 253603 (2023).
- [39] R. Reimann, W. Alt, T. Kampschulte, T. Macha, L. Ratschbacher, N. Thau, S. Yoon, and D. Meschede, Cavity-Modified Collective Rayleigh Scattering of Two Atoms, *Physical Review Letters* **114**, 023601 (2015).
- [40] S. Begley, M. Vogt, G. K. Gulati, H. Takahashi, and M. Keller, Optimized Multi-Ion Cavity Coupling, *Physical Review Letters* **116**, 223001 (2016).
- [41] A. Neuzner, M. Körber, O. Morin, S. Ritter, and G. Rempe, Interference and dynamics of light from a distance-controlled atom pair in an optical cavity, *Nature Photonics* **10**, 303 (2016).
- [42] S. Schütz, S. B. Jäger, and G. Morigi, Thermodynamics and dynamics of atomic self-organization in an optical cavity, *Phys. Rev. A* **92**, 063808 (2015).
- [43] K. J. Arnold, M. P. Baden, and M. D. Barrett, Self-Organization Threshold Scaling for Thermal Atoms Coupled to a Cavity, *Physical Review Letters* **109**, 153002 (2012).
- [44] W. Niedenzu, T. Griebner, and H. Ritsch, Kinetic theory of cavity cooling and self-organisation of a cold gas, *EPL (Europhysics Letters)* **96**, 43001 (2011).
- [45] See supplementary text.
- [46] L. Landau, ON THE THEORY OF PHASE TRANSITIONS, in *Collected Papers of L.D. Landau* (Elsevier, 1965) pp. 193–216.
- [47] X. Zhang, Y. Chen, Z. Wu, J. Wang, J. Fan, S. Deng, and H. Wu, Observation of a superradiant quantum phase transition in an intracavity degenerate Fermi gas, *Science* **373**, 1359 (2021).
- [48] L. Néel, Thermoremanent Magnetization of Fine Powders, *Reviews of Modern Physics* **25**, 293 (1953).
- [49] I. Di Terlizzi, M. Gironella, D. Herrera-Aguilar, T. Betz, F. Monroy, M. Baiesi, and F. Ritort, Variance sum rule for entropy production, *Science* **383**, 971 (2024).
- [50] L. Su, A. Douglas, M. Szurek, A. H. Hebert, A. Krahn, R. Groth, G. A. Phelps, O. Markovic, and M. Greiner, Fast single atom imaging in optical lattice arrays (2024), [arxiv:2404.09978](https://arxiv.org/abs/2404.09978) [cond-mat, physics:physics, physics:quant-ph].
- [51] C. Luo, H. Zhang, V. P. W. Koh, J. D. Wilson, A. Chu, M. J. Holland, A. M. Rey, and J. K. Thompson, Cavity-Mediated Collective Momentum-Exchange Interactions (2023), [arXiv:2304.01411](https://arxiv.org/abs/2304.01411) [physics, physics:quant-ph].
- [52] A. Periwal, E. S. Cooper, P. Kunkel, J. F. Wienand, E. J. Davis, and M. Schleier-Smith, Programmable interactions and emergent geometry in an array of atom clouds, *Nature* **600**, 630 (2021).
- [53] R. M. Kroeze, B. P. Marsh, D. A. Schuller, H. S. Hunt, S. Gopalakrishnan, J. Keeling, and B. L. Lev, Replica symmetry breaking in a quantum-optical vector spin glass (2023), [arxiv:2311.04216](https://arxiv.org/abs/2311.04216) [cond-mat, physics:physics, physics:quant-ph].
- [54] M. Ye, Y. Tian, J. Lin, Y. Luo, J. You, J. Hu, W. Zhang, W. Chen, and X. Li, Universal Quantum Optimization with Cold Atoms in an Optical Cavity, *Physical Review Letters* **131**, 103601 (2023).
- [55] V. Torggler, P. Aumann, H. Ritsch, and W. Lechner, A Quantum N-Queens Solver, *Quantum* **3**, 149 (2019).
- [56] G. Anikeeva, O. Marković, V. Borish, J. A. Hines, S. V. Rajagopal, E. S. Cooper, A. Periwal, A. Safavi-Naeini, E. J. Davis, and M. Schleier-Smith, Number Partitioning With Grover’s Algorithm in Central Spin Systems, *PRX Quantum* **2**, 020319 (2021).
- [57] T. Ilias, D. Yang, S. F. Huelga, and M. B. Plenio, Criticality-Enhanced Quantum Sensing via Continuous Measurement, *PRX Quantum* **3**, 010354 (2022).
- [58] S. Fernández-Lorenzo and D. Porras, Quantum sensing close to a dissipative phase transition: Symmetry breaking and criticality as metrological resources, *Physical Review A* **96**, 013817 (2017).
- [59] M. Tsang, Quantum transition-edge detectors, *Physical Review A* **88**, 021801 (2013).



# Supplementary Material for Optomechanical self-organization in a mesoscopic atom array

Jacquelyn Ho,<sup>1,2</sup> Yue-Hui Lu,<sup>1,2</sup> Tai Xiang,<sup>1,2</sup> Cosimo C. Rusconi,<sup>3</sup> Stuart J. Masson,<sup>3,4</sup> Ana Asenjo-Garcia,<sup>3</sup> Zhenjie Yan,<sup>1,2</sup> and Dan M. Stamper-Kurn<sup>1,2,5,\*</sup>

<sup>1</sup>*Department of Physics, University of California, Berkeley, California 94720*

<sup>2</sup>*Challenge Institute for Quantum Computation, University of California, Berkeley, California 94720*

<sup>3</sup>*Department of Physics, Columbia University, New York, NY 10027*

<sup>4</sup>*Department of Physics, University of South Florida, Tampa, Florida 33620*

<sup>5</sup>*Materials Sciences Division, Lawrence Berkeley National Laboratory, Berkeley, California 94720*

## I. MATERIALS AND METHODS

### A. Atom array preparation

Our tweezer array is created by light at a wavelength of 808 nm that passes through a one-dimensional acousto-optic deflector (AOD), resembling a method described in Ref. [S1]. The tweezer positions are determined by radio-frequency tones, created through an arbitrary waveform generator card, that drive the AOD. The atoms are initially probabilistically loaded into a tweezer array containing 40 sites. We then perform parity projection through polarization gradient cooling (PGC) in a  $\text{lin}\perp\text{lin}$  configuration. The occupation of the sites is determined by fluorescence imaging. Following tweezer loading, we implement two rounds of tweezer rearrangement to bring the loaded atoms into a centered array. Unwanted atoms are dropped by diminishing the optical power in their respective tweezers. We confirm the success of this sorting procedure with an additional fluorescence image. In the event that defects occur during the rearrangement, as noted in images taken before the pumping sequence (see section B), we post-select our data on there being an equal number of even- and odd-indexed sites filled. We take an additional fluorescence image after the pumping sequence and retain only data where the occupancy of the pre- and post-pumping-sequence atom array is identical. This is to ensure that there is no bias in the tweezer positions towards the positive or negative antinodes when we take bifurcation data such as those shown in Fig. 1 and Fig. 2 of the main text.

### B. Pumping sequence and cavity field phase calibration

We use heterodyne detection to measure the cavity field polarized in the  $y$ -direction. Our heterodyne system is schematically shown in Fig. S1. By demodulating the signal from the balanced photodiode at the pump-local oscillator (LO) beat frequency of 20 MHz, we extract both quadratures of the cavity field. Due to the pump and LO emerging from separate fibers, their relative phase  $\phi$  drifts over time, thus necessitating calibration of the phase by referencing it to the field emitted by the atoms. To perform the phase calibration in each shot, we first demodulate the field by applying a fast Fourier transform (FFT) over a  $5\ \mu\text{s}$  period with a Hann window applied. The window is then stepped in  $1\ \mu\text{s}$  increments. The average phase, up to a  $\pi$  rotation, is obtained by performing principal component analysis (PCA) on all data acquired in the shot. To calibrate the cavity field phase in each shot, we use a multi-frame pumping sequence shown in Fig. S2 and described as follows. In frame 1, we initialize the atoms all on the cavity field antinodes with  $5\lambda$  spacing and pump them at a power below the critical point; we define the cavity field phase obtained here as a reference for the phase at the positive antinodes. Then, we move the tweezers into a  $4.5\lambda$  spacing configuration while simultaneously shifting them to the cavity nodes. Next, in frame 2, we pump the atoms with variable power to detect self-organization and symmetry breaking. We take multiple frames in this configuration (typically between 5 and 20 shots) to increase our data-taking rate. Lastly, we shift the atoms back to the antinodes with  $5\lambda$  spacing and obtain another phase reference in the final frame of the sequence by the same method as in frame 1. We observe the phase drift between the first and last reference frames to be less than  $\pi$ . The sign of  $c_{\text{proj}}$  obtained in the middle frames is determined by comparing the phase extracted through PCA to the phase linearly interpolated between the two reference phases; we assume that the PCA phase is less than  $\pi/2$  shifted from the interpolated phase. Example time traces of the cavity field measurement in each frame are shown in Fig. S2. In each frame, we linearly ramp up the

---

\* dmsk@berkeley.edu

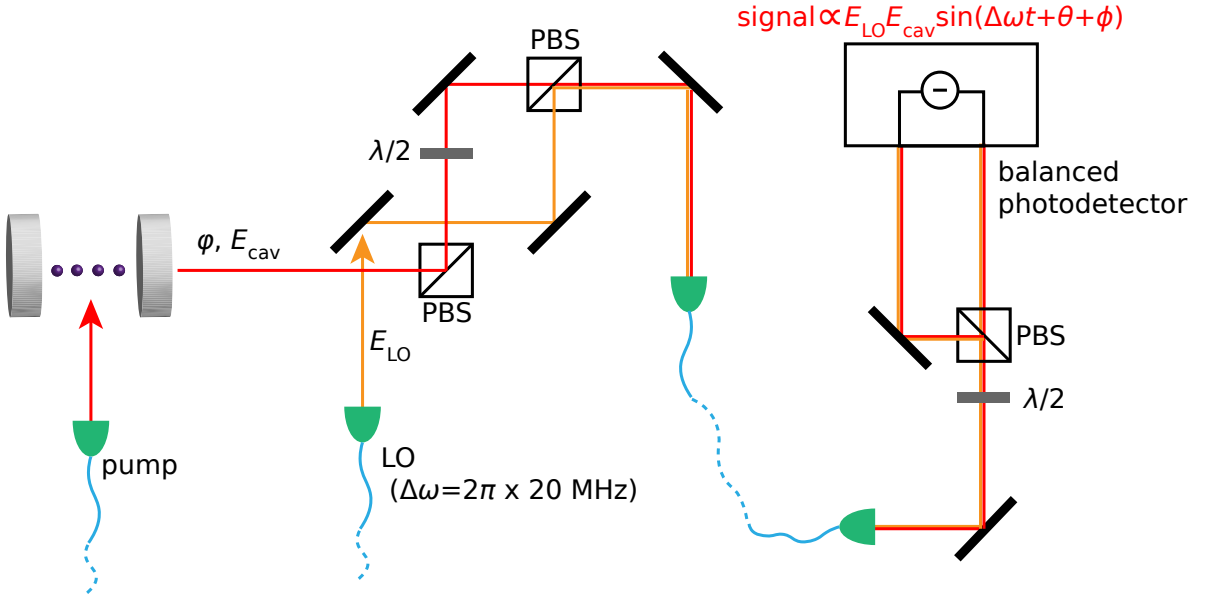


Figure S1. **Schematic of the heterodyne detection system.** The pump and LO beams originate from separate fibers and are combined at a polarizing beamsplitter (PBS) with orthogonal polarizations. They are then both sent into a single mode fiber, which ensures that they are mode-matched at the fiber output. Upon emerging from the fiber, they pass through a half-waveplate (labeled as  $\lambda/2$ ) at  $45^\circ$  and are split at another PBS. Each output port of the last PBS is directed to a sensor on a balanced photodetector, which subtracts the signals on the two sensors. The output voltage of the detector is proportional to  $E_{\text{LO}} E_{\text{cav}} \sin(\Delta\omega t + \theta + \phi)$  where  $E_{\text{LO}}$  is the LO electric field amplitude,  $E_{\text{cav}}$  is the cavity electric field amplitude,  $\Delta\omega = 2\pi \times 20$  MHz is the frequency difference between the pump and LO,  $\phi$  is the phase of the LO relative to the pump, and  $\theta$  is the phase of the cavity field relative to the pump.

pump power to the desired strength in  $50 \mu\text{s}$  and then hold the power constant while simultaneously shining on repump light. Before each frame, we perform 1 ms of PGC to set the initial temperature of the atoms. The  $\sigma^-$ -polarized pump beam optically pumps the atoms into the  $|F = 2, m_F = -2\rangle$  state with the quantization axis along  $x$  during the pump ramp-up. This is done so that when  $\Omega < \Omega_c$ , the atoms stay in  $|F = 2, m_F = -2\rangle$  and no spin dynamics interfere with the spatial self-organization process.

### C. Tweezer position calibration

As noted in the main text, precise control of the tweezer positions with respect to the cavity and pump standing waves is crucial for our experiment. To constrain long-term drift in the position of the array along both the cavity and pump axes, we perform an in-situ measurement of both positions at end of each experimental run, and use the output of this measurement to displace the atom array onto the correct position prior to the start of the next experimental run. For the position measurement, after taking the post-pumping-sequence fluorescence image, we adjust the tweezer spacing (by varying the radio-frequency signal to the AOD) to an equal  $5\lambda$  between neighboring tweezers. For this calibration, we use  $5\lambda$  spacing so that the dominant mode is the center-of-mass mode, which we can easily displace using a piezo-actuated mirror in the tweezer optical path (a method described in Ref. [S2]). This is in contrast to the  $4.5\lambda$  spacing used in the self-organization data shots. We then expose the array to a low-intensity pump field (well below the self-organization transition) simultaneously with PGC light and record the photon emission rate from the cavity. During this recording, the entire array is translated continuously first along the cavity axis and then along the pump axis using the piezo-actuated mirror. The recorded data reveal the sinusoidal variation of the cavity mode and the pump standing wave, respectively. An automated fit applied to these data determines the displacement that must be applied to the atoms to position them properly within the cavity and pump field.

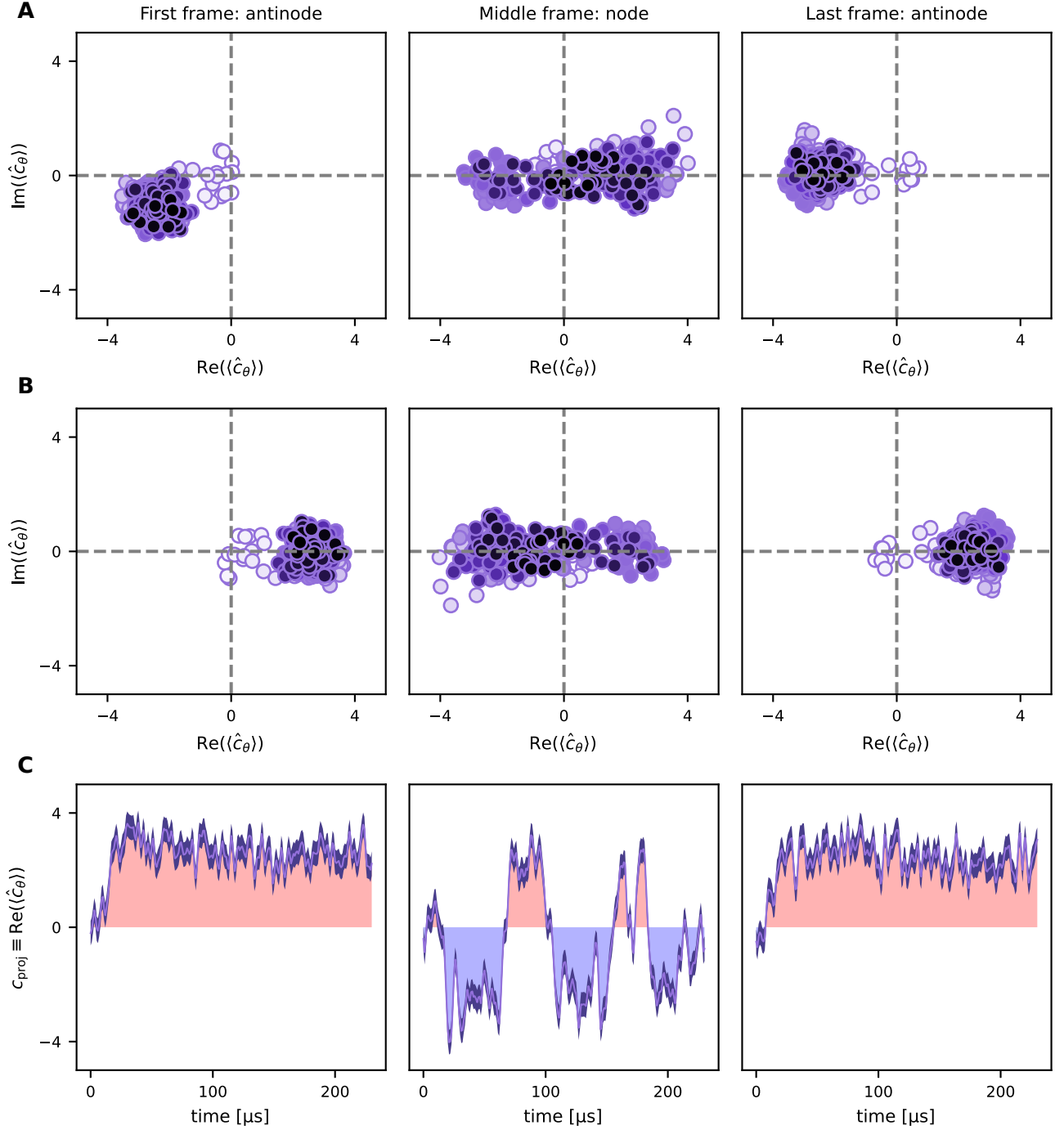


Figure S2. **Example time traces of the detected field in each of the three pumping frames.** (A) Scatter plots of the complex cavity field before phase correction. Each point is obtained by taking the Fourier transform of the heterodyne signal at 20 MHz over  $5 \mu\text{s}$  periods with a Hann window applied. The step time in between points is  $1 \mu\text{s}$ . The real ( $\text{Re}(\langle \hat{c}_\theta \rangle)$ ) and imaginary ( $\text{Im}(\langle \hat{c}_\theta \rangle)$ ) quadratures of the detected field with respect to the average phase of the cavity emission,  $\theta$ , are plotted. Lighter points indicate earlier times and darker points indicate later times. From these data, the angle  $\phi$  of the major axis in each frame is determined by PCA. (B) Detected field after rotation by  $\phi$ . Because PCA only determines the angle of the major axis up to a  $\pi$  rotation, in the antinode frames, we define the average projection of the field onto the axis defined by  $\theta$  to be positive. The sign of the node frame is determined by comparing  $\theta_{\text{node}}$  to the angle linearly interpolated from  $\theta_{\text{first frame}}$  and  $\theta_{\text{last frame}}$  and assuming that the two angles are within  $\pi/2$  of each other. (C) Time traces of  $c_{\text{proj}}$ . Values of  $c_{\text{proj}}$  are obtained by projecting the phase-corrected measurements of  $\hat{c}$  (shown in (B)) onto the  $\theta$ -axis. The shaded dark purple regions indicate the shot noise level. Data shown in figure were taken with  $N = 18$ ,  $\Delta_{\text{pa}} = -2\pi \times 80 \text{ MHz}$ ,  $\Delta_{\text{pc}} = -2\pi \times 2.15 \text{ MHz}$ , and  $\Omega = 2\pi \times 63.9 \text{ MHz}$ .

## II. SUPPLEMENTARY TEXT

### A. Theoretical Model

The theoretical prediction of the critical drive strength is derived from an effective two dimensional model where the atoms move along and perpendicular to the cavity axis ( $z$ -axis). Of the two directions perpendicular to the cavity axis, we consider the one ( $x$ -axis) along the direction of the pump. Motional effects along the remaining direction can be neglected as the beam waist of the pump is much larger than the spread of the atomic wavefunction. Each tweezer trap is approximated by a harmonic potential, and the atoms are assumed to be two-level systems of mass  $M$ . The degrees of freedom of the system are thus the internal ground  $|g\rangle$  and excited  $|e\rangle$  states of the atoms, the position  $\hat{z}_j, \hat{x}_j$  and momentum  $\hat{p}_{zj}, \hat{p}_{xj}$  operators of each atom, and the cavity field described by the bosonic creation  $\hat{c}^\dagger$  and annihilation  $\hat{c}$  operators for a photon in the cavity. The dynamics of the system obeys the master equation

$$\dot{\hat{\rho}}_{\text{tot}} = -\frac{i}{\hbar} [\hat{H}_{\text{tot}}, \hat{\rho}_{\text{tot}}] + \kappa (2\hat{c}\hat{\rho}_{\text{tot}}\hat{c}^\dagger - \{\hat{c}^\dagger\hat{c}, \hat{\rho}_{\text{tot}}\}) + \gamma \sum_j \left( 2 \int d\mathbf{n} \mathcal{N}(\mathbf{n}) e^{-ik_0\mathbf{n}\cdot\hat{\mathbf{r}}_j} \hat{\sigma}_j^- \hat{\rho}_{\text{tot}} e^{ik_0\mathbf{n}\cdot\hat{\mathbf{r}}_j} \hat{\sigma}_j^+ - \{\hat{\sigma}_j^+ \hat{\sigma}_j^-, \hat{\rho}_{\text{tot}}\} \right), \quad (\text{S1})$$

where  $\hat{\sigma}_j^\pm \equiv |e_j\rangle\langle g_j| = (\hat{\sigma}_j^\mp)^\dagger$  are the atomic coherence operators. The second term in Eq. (S1) describes the decay of the cavity field, where  $\kappa$  is the cavity half-linewidth. The last term describes the atomic decay into free space including recoil effects. Here,  $k_0 = \omega_a/c$ ,  $\gamma$  is the atomic half-linewidth,  $\mathcal{N}(\mathbf{n})$  is the dipole emission pattern, and the integral is taken over all directions in space represented by the unit vector  $\mathbf{n}$ . We define the position operator for the atom  $j$  in the  $xz$ -plane as  $\hat{\mathbf{r}}_j = (\hat{x}_j, \hat{z}_j)$ . The Hamiltonian that describes the coupling between the atoms and the cavity, written in the frame rotating at the frequency of the pump  $\omega_p$ , reads

$$\hat{H}_{\text{tot}} \equiv \sum_{j=1}^N \left\{ \frac{\hat{\mathbf{p}}_j^2}{2M} + \frac{M\nu^2}{2} [(\hat{z}_j - z_{0j})^2 + \hat{x}_j^2] - \hbar\Delta_{\text{pa}}\hat{\sigma}_j^+\hat{\sigma}_j^- + \frac{\hbar\Omega(\hat{x}_j)}{2}(\hat{\sigma}_j^+ + \hat{\sigma}_j^-) + \hbar g_0 \sin(k\hat{z}_j) (\hat{c}^\dagger \hat{\sigma}_j^- + \hat{\sigma}_j^+ \hat{c}) \right\} - \hbar\Delta_{\text{pc}}\hat{c}^\dagger\hat{c}. \quad (\text{S2})$$

Here,  $\Delta_{\text{pc}} \equiv \omega_p - \omega_c$  and  $\Delta_{\text{pa}} \equiv \omega_p - \omega_a$  are the pump detunings from the cavity frequency ( $\omega_c$ ) and atomic frequency ( $\omega_a$ ) respectively, and  $\nu$  is the trap frequency of the tweezers. We assume the foci of the tweezers lie parallel to the cavity axis, where  $z_{0j}$  is the position of the tweezer trap for the  $j$ -th atom. We approximate the spatial profile of the cavity field as  $\sin(kz)$ , with wave vector  $k = 2\pi/\lambda$ . The side pump driving the atoms consists of two counter propagating beams, which result in a standing wave profile  $\Omega(x) = \Omega \cos(k_p x)$  whose maximum is located at the position of the atoms. Here,  $k_p \simeq k$  is the pump wave-vector. We assume the atoms to be driven in phase, which is achieved by aligning the atomic array orthogonal to the pump direction.

The experiment is operated in the limit of large pump-atom detuning,  $\Delta_{\text{pa}} \gg \{g_0, \Omega, \kappa, \gamma\}$ . Hence, we adiabatically eliminate the internal atomic degrees of freedom assuming linear response (that is  $\langle \hat{\sigma}_j^\pm \rangle \simeq -1$ ) and neglecting atomic free-space decay. Within this approximation, the dynamics of the system obeys the effective master equation

$$\partial_t \hat{\rho}_{\text{om}} = -\frac{i}{\hbar} [\hat{H}_{\text{om}}, \hat{\rho}] + \kappa (2\hat{c}\hat{\rho}_{\text{om}}\hat{c}^\dagger - \{\hat{c}^\dagger\hat{c}, \hat{\rho}_{\text{om}}\}), \quad (\text{S3})$$

where  $\hat{\rho}_{\text{om}}$  describes the state of the atomic motion and of the cavity field. The second term in Eq. (S3) represents the damping of the cavity, and the effective optomechanical Hamiltonian that describes the coupling of the atomic motion to the cavity field reads

$$\begin{aligned} \hat{H}_{\text{om}} = & \sum_{j=1}^N \left\{ \frac{\hat{\mathbf{p}}_j^2}{2M} + \frac{M}{2}\nu^2 [\hat{x}_j^2 + (\hat{z}_j - z_{0j})^2] - \frac{\hbar\Omega^2}{4\Delta_{\text{pa}}} \cos^2(k\hat{x}_j) \right\} - \hbar\Delta_{\text{pc}}\hat{c}^\dagger\hat{c} \\ & + \frac{\hbar g_0}{2\Delta_{\text{pa}}} (\hat{c}^\dagger + \hat{c}) \sum_{j=1}^N \Omega(\hat{x}_j) \sin(k\hat{z}_j) + \frac{\hbar g_0^2}{\Delta_{\text{pa}}} \hat{c}^\dagger \hat{c} \sum_{j=1}^N \sin^2(k\hat{z}_j), \end{aligned} \quad (\text{S4})$$

The optomechanical coupling is described by the first and second terms in the second line of Eq. (S4). The latter is the well-known coupling arising from radiation pressure forces and is common to several optomechanical systems [S3]. It describes the dispersive shift of the cavity frequency due to the atoms and the back-action of the cavity on the atomic trap frequency (known as the ‘‘optical spring effect’’). The former, instead, arises from the coherent scattering of photons from the pump into the cavity and so depends on the Rabi frequency of the pump [S4–S6]. This term produces a force proportional to the cavity field that shifts the atomic equilibrium position away from the nodes.

These two coupling terms can be tuned independently. In particular, by changing the Rabi frequency of the pump  $\Omega$  while keeping the ratio  $g_0/\Delta_{\text{pa}}$  fixed, one can make the coherent scattering dominate over the radiation pressure coupling.

We remark that a very similar model has been considered for driven atomic clouds in optical cavities, considered for instance in Refs. [S7–S10]. The difference here is given by the tweezer traps, which add an additional time-scale of the order  $1/\nu$  for the motional dynamics of the atoms. As we will see below, this leads to a change in the critical pump strength ( $\Omega_c$ ) responsible for atomic self-organization. This model is justified for values of  $\Omega$  below and around the transition point where atomic saturation is negligible. Above the transition ( $\Omega > \Omega_c$ ), the buildup of the cavity field leads to non-negligible saturation of the atoms, and to diffusion of the internal excitation to other internal levels. This latter effect leads to the breakdown of the two-level approximation for the atoms. However, the model is sufficient for the purpose of deriving the value of the critical pump strength  $\Omega_c$  as we now discuss.

## B. Derivation of the critical pump strength $\Omega_c$

In the absence of the pump ( $\Omega = 0$ ) and with tweezers placed at the cavity field nodes, i.e.  $z_{0j} = jn\lambda$  for any integer or half integer  $n$ , the steady state solution of Eq. (S3) corresponds to the cavity in vacuum and the atoms in the thermal state of the harmonic tweezers potential. As  $\Omega$  is increased, the atoms start to scatter photons into the cavity, which act back on the atoms modifying the effective trap frequency. At the critical value  $\Omega_c$ , the solution of atoms at the nodes becomes unstable, leading to self-organization towards the cavity antinodes for  $\Omega > \Omega_c$ . To compute  $\Omega_c$ , we take a mean field approach where correlations between the cavity and the atomic motion are neglected [S11]. It is instructive to first consider the case where atoms are allowed to move only along the cavity axis. In the following we thus consider an effective one-dimensional model for the atomic motion. We will later generalize the results to two dimensions.

### 1. 1D Motion

The effective optomechanical model for atoms moving along the cavity axis only is obtained from Eq. (S3) assuming  $\Omega(x) = \Omega$  in Eq. (S4). According to the mean field approximation, we consider the system dynamics to be confined to the product state manifold defined by

$$\hat{\rho}_{\text{MF}} = |\alpha\rangle\langle\alpha| \otimes \hat{\rho}_{\text{at}}, \quad (\text{S5})$$

where  $\hat{\rho}_{\text{at}}$  is the density matrix of the atomic motion, and  $|\alpha\rangle$  the coherent state of the cavity field. In this case, the evolution of the atomic motional state reads

$$\dot{\hat{\rho}}_{\text{at}} = -\frac{i}{\hbar} [\hat{H}_{1\text{D}}, \hat{\rho}_{\text{at}}] - i \frac{\Omega g_0}{2\Delta_{\text{pa}}} (\alpha + \alpha^*) \left[ \sum_{j=1}^N \sin(k\hat{z}_j), \hat{\rho}_{\text{at}} \right] - i |\alpha|^2 \frac{g_0^2}{\Delta_{\text{pa}}} \left[ \sum_{j=1}^N \sin^2(k\hat{z}_j), \hat{\rho}_{\text{at}} \right], \quad (\text{S6})$$

where we defined the field amplitude  $\alpha \equiv \langle \hat{c} \rangle$ , and the Hamiltonian  $\hat{H}_{1\text{D}} \equiv \sum_j [\hat{p}_j^2/2M + M\nu^2(\hat{z}_j - z_{0j})^2/2]$ . The evolution of the average cavity field  $\alpha$  depends on the mean field dynamics of the  $N$  atoms and reads

$$\dot{\alpha} = \left[ i \left( \Delta_{\text{pc}} - \frac{g_0^2}{\Delta_{\text{pa}}} \sum_{j=1}^N \langle \sin^2(k\hat{z}_j) \rangle \right) - \kappa \right] \alpha - i \frac{g_0 \Omega}{2\Delta_{\text{pa}}} \left\langle \sum_{j=1}^N \sin(k\hat{z}_j) \right\rangle, \quad (\text{S7})$$

where  $\langle \cdot \rangle = \text{Tr}[\cdot \hat{\rho}_{\text{at}}]$ . We proceed to linearize the system around the solution in Eq. (S5) with  $\alpha = 0$  and where each atom is in the thermal state  $\hat{\rho}_{\text{th}} \equiv \exp(-\beta \hat{H}_{1\text{D}})/\mathcal{Z}$ , with  $\beta = 1/k_B T$  and  $\mathcal{Z} \equiv \text{Tr}[\exp(-\beta \hat{H}_{1\text{D}})]$ . Accordingly, we make the substitution  $\alpha \rightarrow \delta\alpha$  and  $\hat{\rho}_{\text{at}} \rightarrow \hat{\rho}_{\text{th}} + \delta\hat{\rho}$  in Eqs. (S6) and (S7), and keep only terms linear in the fluctuations. We readily find

$$\begin{aligned} \delta\dot{\hat{\rho}} &= \mathcal{L}_0 \delta\hat{\rho} - i \frac{\Omega g_0}{2\Delta_{\text{pa}}} (\delta\alpha + \delta\alpha^*) \left[ \sum_{j=1}^N \sin(k\hat{z}_j), \hat{\rho}_{\text{th}} \right], \\ \delta\dot{\alpha} &= \left[ i \left( \Delta_{\text{pc}} - \frac{g_0^2}{\Delta_{\text{pa}}} \sum_{j=1}^N \langle \sin^2(k\hat{z}_j) \rangle_{\text{th}} \right) - \kappa \right] \delta\alpha - i \frac{g_0 \Omega}{2\Delta_{\text{pa}}} \text{Tr} \left[ \sum_{j=1}^N \sin(k\hat{z}_j) \delta\hat{\rho} \right]. \end{aligned} \quad (\text{S8})$$

Here, we defined the superoperator  $\mathcal{L}_0\hat{\rho} \equiv -i\hbar^{-1}[\hat{H}_{1D}, \hat{\rho}]$ , and  $\langle \cdot \rangle_{\text{th}} \equiv \text{Tr}[\cdot \hat{\rho}_{\text{th}}]$  for convenience of notation.

The critical pump strength  $\Omega_c$  corresponds to the pole of the susceptibility of the system [S11, S12]. To compute the susceptibility, we take the Laplace transform of Eq. (S8). We define  $\tilde{\hat{\rho}} = \int_0^\infty dt e^{-st} \delta\hat{\rho}(t)$  and  $\tilde{\alpha} = \int_0^\infty dt e^{-st} \delta\alpha(t)$ , where  $s = -i\omega + \epsilon$ , with  $\epsilon > 0$  to ensure the analyticity of the susceptibility in the upper-half complex plane [S12]. The Laplace transform of the atomic operator reads

$$\tilde{\hat{\rho}} = (s\mathbb{I} - \mathcal{L}_0)^{-1} \delta\hat{\rho}(0) - i\frac{g_0\Omega}{2\Delta_{\text{pa}}} (\tilde{\alpha} + \tilde{\alpha}^*) (s\mathbb{I} - \mathcal{L}_0)^{-1} \left[ \sum_{j=1}^N \sin(k\hat{z}_j), \hat{\rho}_{\text{th}} \right], \quad (\text{S9})$$

where  $\mathbb{I}$  is the identity superoperator, and  $\delta\hat{\rho}(0)$  is the initial condition of the linear fluctuation of the atomic density operator. Substituting Eq. (S9) into the equation for the cavity field we obtain the solution

$$\mathcal{A}(s)\tilde{\alpha} + \mathcal{C}(s)\tilde{\alpha}^* = \alpha(0) - i\frac{g_0\Omega}{2\Delta_{\text{pa}}} N \text{Tr} \left\{ \sum_{j=1}^N \sin(k\hat{z}_j) (s - \mathcal{L}_0)^{-1} \delta\hat{\rho}(0) \right\}, \quad (\text{S10})$$

where  $\alpha(0)$  is the initial condition for the cavity field fluctuations and we have defined

$$\mathcal{A}(s) \equiv s - i\left(\Delta_{\text{pc}} - \frac{g_0^2}{\Delta_{\text{pa}}} \sum_{j=1}^N \langle \sin^2(k\hat{z}_j) \rangle_{\text{th}}\right) + \kappa + \mathcal{C}(s), \quad (\text{S11})$$

and

$$\begin{aligned} \mathcal{C}(s) &= \left(\frac{g_0\Omega N}{2\Delta_{\text{pa}}}\right)^2 \text{Tr} \left\{ \hat{\Theta} (s\mathbb{I} - \mathcal{L}_0)^{-1} [\hat{\Theta}, \hat{\rho}_{\text{th}}] \right\} = \left(\frac{g_0\Omega N}{2\Delta_{\text{pa}}}\right)^2 \int_0^\infty dt e^{-st} \text{Tr} \left\{ \hat{\Theta} e^{\mathcal{L}_0 t} [\hat{\Theta}, \hat{\rho}_{\text{th}}] \right\} \\ &= \left(\frac{g_0\Omega N}{2\Delta_{\text{pa}}}\right)^2 \int_0^\infty dt e^{-st} \langle [\hat{\Theta}(t), \hat{\Theta}] \rangle_{\text{th}}, \end{aligned} \quad (\text{S12})$$

where we defined the operator

$$\hat{\Theta} \equiv \frac{1}{N} \sum_{j=1}^N \sin(k\hat{z}_j). \quad (\text{S13})$$

In Eq. (S12), we employed the Laplace transform identity  $(s\mathbb{I} - \mathcal{L}_0)^{-1} = \int_0^\infty dt e^{-(s\mathbb{I} - \mathcal{L}_0)t}$  in the first passage. From the first to the second line, we used the adjoint action of the operator  $\exp(\mathcal{L}_0 t)$  to transform the Schrödinger operator  $\hat{\Theta}$  into the Heisenberg operator  $\hat{\Theta}(t)$ . Note that  $\hat{\Theta} = \hat{\Theta}(0)$ .

These equations have a simple physical interpretation. The correlator appearing in Eq. (S12) corresponds to the linear response function of the operator  $\hat{\Theta}$  [S12] that defines the mechanical response to the force exerted by the scattering of photons into the cavity. From Eq.(S11), we interpret  $\mathcal{C}(s)$  as the effective shift to the cavity response due to the backaction of the atoms on the cavity field arising from coherent scattering. The appearance of the operator  $\hat{\Theta}$  indicates that this shift depends on the collective self organization of the atoms. Additionally, the non-linear dependence on  $\hat{z}$  accounts for the non-linear correction to the mechanical response of the system as we shall see below.

The dynamics of the cavity field is thus found by solving the following system of equations and taking the inverse Laplace transform

$$R(s) \begin{pmatrix} \tilde{\alpha} \\ \tilde{\alpha}^* \end{pmatrix} = \begin{pmatrix} \alpha(0) - i\frac{g_0\Omega}{2\Delta_{\text{pa}}} \text{Tr} \left[ \hat{\Theta} (s\mathbb{I} - \mathcal{L}_0)^{-1} \delta\hat{\rho}(0) \right] \\ \alpha^*(0) + i\frac{g_0\Omega}{2\Delta_{\text{pa}}} \text{Tr} \left[ \hat{\Theta} (s\mathbb{I} - \mathcal{L}_0)^{-1} \delta\hat{\rho}(0) \right]^* \end{pmatrix}, \quad (\text{S14})$$

where

$$R(s) \equiv \begin{pmatrix} \mathcal{A}(s) & \mathcal{C}(s) \\ \mathcal{C}^*(s) & \mathcal{A}^*(s) \end{pmatrix} \quad (\text{S15})$$

is related to the inverse response function of the cavity field. The crossover between stable and unstable behaviour occurs when the susceptibility diverges. The susceptibility of the cavity field to the coherent scattering of photon by

the atoms is defined as the the response function of the cavity at zero frequency [S12]. Accordingly, the crossover occurs when  $\det[R(0)] = 0$ . This happens when the following condition is met

$$\Delta_{\text{pc}}^2(T) + \kappa^2 - 2\Delta_{\text{pc}}(T)\text{Im}[\mathcal{C}(0)] + 2\kappa\text{Re}[\mathcal{C}(0)] = 0. \quad (\text{S16})$$

Here  $\mathcal{C}(0) \equiv \lim_{\epsilon \rightarrow 0^+} \mathcal{C}(-i\omega + \epsilon)|_{\omega=0}$ . In the above expression, the effective cavity shift reads

$$\Delta_{\text{pc}}(T) \equiv \Delta_{\text{pc}} - \frac{g_0^2 N}{\Delta_{\text{pa}}} \langle \sin^2(k\hat{z}) \rangle_{\text{th}} = \Delta_{\text{pc}} - \frac{g_0^2 N}{2\Delta_{\text{pa}}} \left(1 - e^{-2\eta_T^2}\right). \quad (\text{S17})$$

The second term on the right hand side of Eq. (S17) represents the frequency shift of the cavity due to thermal fluctuations of the atoms in the initial state  $\hat{\rho}_{\text{th}}$ . Here, we defined the thermal Lamb-Dicke parameter as

$$\eta_T \equiv \eta \sqrt{\coth\left(\frac{\hbar\nu}{2k_B T}\right)}, \quad (\text{S18})$$

where  $\eta \equiv \sqrt{\nu_R/\nu}$  is the Lamb-Dicke parameter for an atom in the motional ground state and  $\nu_R \equiv \hbar k^2/2M$  is the recoil frequency of the atom.

To evaluate the condition in Eq. (S16), we need to compute  $\mathcal{C}(0)$ , which corresponds to the susceptibility of the operator  $\hat{\Theta}$ . This is given by

$$\mathcal{C}(0) = \left(\frac{g_0 \Omega N}{2\Delta_{\text{pa}}}\right)^2 \lim_{\epsilon \rightarrow 0^+} \int_0^\infty dt e^{-\epsilon t} \langle [\hat{\Theta}(t), \hat{\Theta}] \rangle_{\text{th}}. \quad (\text{S19})$$

For a tweezer trap frequency  $\nu/2\pi \simeq 93$  kHz and for an initial temperature  $T \simeq 40\mu\text{K}$ , the Lamb-Dicke parameter  $\eta_T \simeq 0.8$  is too large to make any perturbative approximation. We thus need to evaluate the response function of  $\hat{\Theta}$  exactly. We first proceed to notice that  $\hat{\rho}_{\text{th}}$  is a product state where each atom is in a thermal state. Hence we can write

$$\langle [\hat{\Theta}(t), \hat{\Theta}] \rangle_{\text{th}} = \frac{1}{N} \langle [\sin(k\hat{z}(t)), \sin(k\hat{z})] \rangle_{\text{th}}, \quad (\text{S20})$$

where  $\hat{z}$  is the position operator of a generic single atom, and we dropped the index  $j$  for convenience. Since  $\hat{z}(t) = \hat{z} \cos(\nu t) + \hat{p} \sin(\nu t)/(M\nu)$ , we use the Baker-Campbell-Hausdorff lemma to evaluate the commutator, finding

$$[\sin(k\hat{z}(t)), \sin(k\hat{z})] = -i \sin(\nu t) \{ \cos[k\hat{z} - k\hat{z}(t)] + \cos[k\hat{z} + k\hat{z}(t)] \}. \quad (\text{S21})$$

The average over the thermal state of Eq. (S21) can be easily computed using the Wigner function representation of the thermal state. Putting everything together, we obtain

$$\begin{aligned} \mathcal{C}(0) &= -2ie^{-\eta_T^2} \left(\frac{g_0 \Omega}{2\Delta_{\text{pa}}}\right)^2 N \lim_{\epsilon \rightarrow 0^+} \int_0^\infty dt e^{-\epsilon t} \sin[\eta_T^2 \sin(\nu t)] \cosh[\eta_T^2 \cos(\nu t)] \\ &\simeq -2i\eta^2 e^{-\eta_T^2} \left(\frac{g_0 \Omega}{2\Delta_{\text{pa}}}\right)^2 N \lim_{\epsilon \rightarrow 0^+} \int_0^\infty dt e^{-\epsilon t} \sin(\nu t) \cosh[\eta_T^2 \cos(\nu t)], \end{aligned} \quad (\text{S22})$$

where information of the motional temperature appears through the Lamb-Dicke parameter  $\eta_T$ , and in going from the first to the second line we kept the leading order in  $\eta^2$ . The resulting integral in Eq. (S22) can be computed exactly by means of the identity

$$\cosh[\eta_T^2 \cos(\nu t)] = I_0(\eta_T^2) + 2 \sum_{n=1}^{\infty} I_{2n}(\eta_T^2) \cos(2n\nu t), \quad (\text{S23})$$

where  $I_n(x)$  is  $n$ -th order modified Bessel function of the first kind. We can compute  $\mathcal{C}(0)$  by substituting Eq. (S23) into Eq. (S22) performing the integral and taking the limit  $\epsilon \rightarrow 0^+$ . Substituting this result into Eq. (S16) and solving for the pump strength we obtain the critical pump strength

$$\Omega_c \equiv \sqrt{\frac{\nu \Delta_{\text{pa}}^2 (\Delta_{\text{pc}}^2(T) + \kappa^2)}{\eta^2 g_0^2 |\Delta_{\text{pc}}(T)| N \epsilon_{1D}(T)}}, \quad (\text{S24})$$

where

$$\varepsilon_{1D}(T) = e^{-\eta_T^2} \left[ I_0(\eta_T^2) + 2 \sum_{n=1}^{\infty} \frac{I_{2n}(\eta_T^2)}{1 - 4n^2} \right] \approx e^{-\eta_T^2} \frac{\sinh \eta_T^2}{\eta_T^2}. \quad (\text{S25})$$

The last equality has not been formally derived. It has been obtained by expanding the modified Bessel functions up to high orders in  $\eta_T$  and noticing the agreement with the Taylor expansion of the hyperbolic sine function.

We conclude this section with several remarks. First, the critical pump strength in Eq. (S24) includes both the effects of finite motional temperature of the atoms as well as the effects of non-linearities in the atomic motion resulting from the interaction with the cavity field in Eq. (S4). Had we neglected the non-linearities in the effective atomic potential, we would have obtained  $\varepsilon_{1D}(T) = 1$ . The main consequence of the motional non-linearities is thus to shift the critical pump strength to higher values. Second, the effects of the temperature are two-fold. On the one hand, it shifts the cavity resonance through  $\Delta_{pc}(T)$ . On the other hand, it leads the atoms to probe the non-linear potential through the thermal spread of the the atomic wavefunction. Accordingly, when the temperature is sufficiently low, the dynamics can be approximated as linear. In this case, and to linear order in the displacement from equilibrium, only one collective mode is coupled to the cavity field. We call this mode the dominant mode [S13]. The critical pump strength can then be understood as the value at which the dominant mode becomes unstable. Finally, this insight leads to an alternative interpretation to the thermal effects and the role of non-linearities. The thermal shift in  $\varepsilon_{1D}(T)$  arises from the sum of two different contributions. One is the non-linear correction to the potential of the dominant mode that contributes with  $\varepsilon_{1D}(T)/N$ . The other is the correction arising from the occupation of the other  $N - 1$  normal modes which couple to the dominant mode via the non-linearities. Each of these modes also contributes  $\varepsilon_{1D}(T)/N$  due to equipartition. The dominant mode thus couples to a bath of modes to which it can disperse energy. This results in an increase in the effective pump strength  $\Omega_c$  required to observe the crossover to self-organization.

## 2. 2D Motion

We now generalize the result to the case of atoms moving both along and perpendicular to the cavity axis. The coupled mean field equation for the cavity and atomic motional state read

$$\begin{aligned} \dot{\hat{\rho}}_{\text{at}} &= -\frac{i}{\hbar} [\hat{H}_{2D}, \hat{\rho}_{\text{at}}] - i \frac{\Omega g_0}{2\Delta_{\text{pa}}} (\alpha + \alpha^*) \left[ \sum_{j=1}^N \cos(k\hat{x}_j) \sin(k\hat{z}_j), \hat{\rho}_{\text{at}} \right] - i |\alpha|^2 \frac{g_0^2}{\Delta_{\text{pa}}} \left[ \sum_{j=1}^N \sin^2(k\hat{z}_j), \hat{\rho}_{\text{at}} \right], \\ \dot{\alpha} &= \left[ i \left( \Delta_{\text{pc}} - \frac{g_0^2}{\Delta_{\text{pa}}} \sum_{j=1}^N \langle \sin^2(k\hat{z}_j) \rangle \right) - \kappa \right] \alpha - i \frac{g_0 \Omega}{2\Delta_{\text{pa}}} \left\langle \sum_{j=1}^N \cos(k\hat{x}_j) \sin(k\hat{z}_j) \right\rangle, \end{aligned} \quad (\text{S26})$$

where

$$\hat{H}_{2D} \equiv \sum_j \left\{ \frac{\hat{\mathbf{p}}_j^2}{2M} + \frac{M\nu^2}{2} [(\hat{z}_j - z_{0j})^2 + \hat{x}_j^2] - \frac{\hbar\Omega^2}{4\Delta_{\text{pa}}} \cos^2(k\hat{x}_j) \right\}, \quad (\text{S27})$$

and  $\hat{\mathbf{p}}_j = (\hat{p}_{xj}, \hat{p}_{zj})$ . Proceeding in the same way as for the 1D case, we obtain the same condition of Eq. (S16) for the poles of the cavity susceptibility, but with  $\mathcal{C}(s)$  substituted by

$$\mathcal{C}_{2D}(s) = \left( \frac{g_0 \Omega}{2\Delta_{\text{pa}}} \right)^2 N \lim_{\epsilon \rightarrow 0^+} \int_0^{\infty} dt e^{-\epsilon t} \langle [\cos(k\hat{x}(t)) \sin(k\hat{z}(t)), \cos(k\hat{x}) \sin(k\hat{z})] \rangle_{\text{th}}. \quad (\text{S28})$$

Since the initial thermal state is factorized, we have written Eq. (S28) in terms of the average over a single atom. In this case, the evolution of  $\hat{x}(t)$  is governed by the harmonic potential of the tweezer and the  $\cos^2(k\hat{x})$  potential corrections introduced by the standing wave of the side pump, as shown in Eq. (S27). If we approximate the cosine potential as  $\cos^2(k\hat{x}) \simeq 1 - (k\hat{x})^2$ , we obtain the leading correction to the trap frequency along the  $x$ -axis as a function of the pump strength. In this case, it is possible to obtain a closed expression for Equation (S28) by following the same steps and approximations we illustrated for the case of motion along a single direction. However, the resulting expression for the critical pump strength is given in terms of an implicit function of  $\Omega$  whose zeros correspond to  $\Omega_c$ . The difficulty of obtaining an explicit expression for  $\Omega_c$  follows from the fact that the Lamb-Dicke parameters and trap frequency for the motion along the  $x$ -axis depend on  $\Omega$ . To obtain a close expression for  $\Omega_c$ , we thus neglect the shift induced by the pump on the trap frequency along the  $x$ -axis. While this approximation seems *a priori* not justified, we



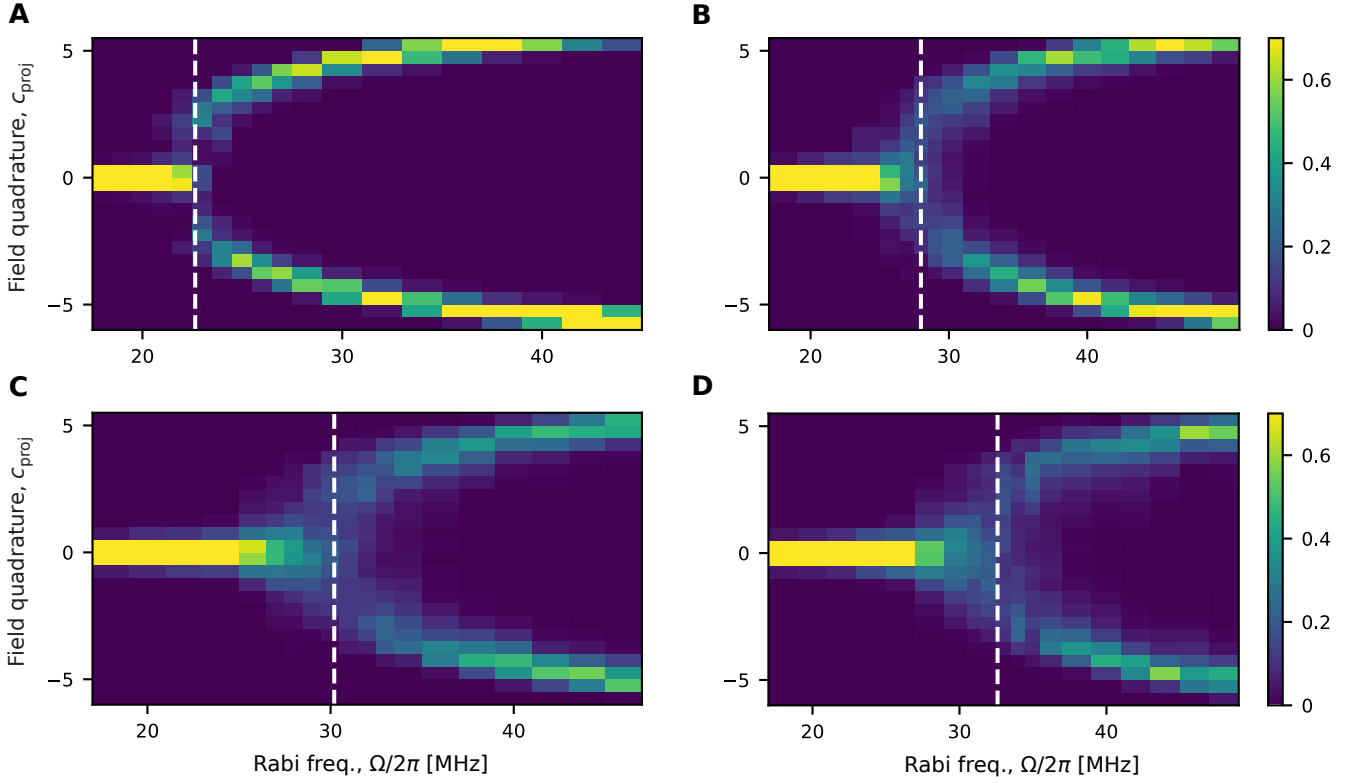


Figure S3. Numerical results of the bifurcation diagram for the field projection as computed from Eqs. (S30a-S30g) for different motional temperatures: **(A)**  $T = 20 \mu\text{K}$ , **(B)**  $T = 41 \mu\text{K}$ , **(C)**  $T = 50 \mu\text{K}$  and **(D)**  $T = 60 \mu\text{K}$ . The white dashed vertical line corresponds to the analytical prediction from the 2D model. The parameters  $N = 20$ ,  $\Delta_{\text{pa}} = -2\pi \times 80 \text{ MHz}$ , and  $\Delta_{\text{pc}} = -2\pi \times 1.9 \text{ MHz}$  are the same for all subplots. The color bar shows the probability density.

check that the final result agrees with the numerical simulations where this effect is included [see Sec. II C]. Neglecting this  $\Omega$ -dependent shift, one obtains the same expression for the critical pump strength as in 1D, i.e., Eq. (S24), but where now  $\varepsilon_{1\text{D}}(T)$  is substituted by

$$\varepsilon(T) \equiv e^{-2\eta_T^2} \left[ I_0(2\eta_T^2) + 2 \sum_{n=1}^{\infty} \frac{I_{2n}(2\eta_T^2)}{1-4n^2} \right] \approx e^{-2\eta_T^2} \frac{\sinh[2\eta_T^2]}{2\eta_T^2}. \quad (\text{S29})$$

Within these approximations, the only modification induced by the additional motional direction is to double the contribution of the thermal Lamb-Dicke parameter.

### C. Numerical simulation of the mean-field semiclassical dynamics

We also compute the bifurcation diagram for the cavity field output by solving the semiclassical equations for the evolution of the expectation value of the system's degrees of freedom in Eq. (S1). Specifically, we numerically solve

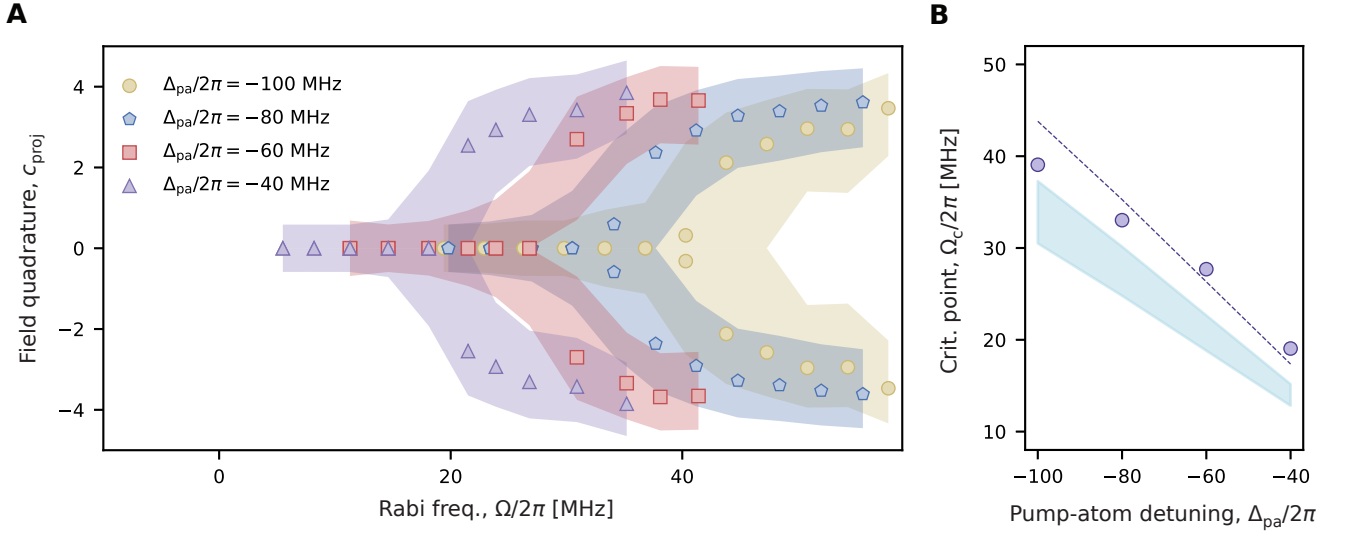


Figure S4. **Dependence of the critical point on  $\Delta_{pa}$ .** (A) Data showing the bifurcation for 20 atoms at four values of  $\Delta_{pa}$ . Markers represent the maxima of the fitted Boltzmann probability distribution of  $c_{proj}$ . Shaded areas show the width of the distribution at half-maximum. Different pump-cavity detunings were chosen for each setting of  $\Delta_{pa}$  to compensate for the different dispersive shifts on the cavity resonance frequency for 20 atoms placed at the nodes. The values used are  $\Delta_{pc} = -2\pi \times \{1.79, 1.9, 2.02, 2.26\}$  MHz corresponding to  $\Delta_{pa} = -2\pi \times \{100, 80, 60, 40\}$  MHz. These correspond approximately to  $\Delta_{pc}(T) \simeq -2\pi \times 1.6$  MHz when accounting for the shift that thermal atoms put on the cavity resonance frequency. (B) Extracted  $\Omega_c$  (circles) exhibit an approximately linear dependence on  $\Delta_{pa}$ . The dashed line shows a fit to Equation (4) in the main text, which gives a fitted temperature of  $T = 66 \pm 8 \mu\text{K}$ . The shaded region shows the prediction of Equation (4) for the independent temperature measurement. Error bars are smaller than the markers.

the following set of equations

$$\partial_t \sigma_n^z = -2\gamma (1 + \sigma_j^z) + i\Omega(x) (\sigma_j^- - \sigma_j^+) + 2ig_0 \sin(kz_j) (\sigma_j^- c^* - \sigma_j^+ c), \quad (\text{S30a})$$

$$\partial_t \sigma_n^- = \Delta_A \sigma_j^- + i \left[ \frac{\Omega(x)}{2} + g_0 \sin(kz_j) c \right] \sigma_j^z, \quad (\text{S30b})$$

$$\partial_t c = \Delta_C c - ig_0 \sum_{j=1}^N \sin(kz_j) \sigma_j^-, \quad (\text{S30c})$$

$$\partial_t p_{zj} = -Mv^2 z_j - \hbar k g_0 \cos(kz_j) (c^* \sigma_j^- + c \sigma_j^+), \quad (\text{S30d})$$

$$\partial_t p_{xj} = -Mv^2 x_j - \frac{1}{2} \partial_x \Omega(x) (\hat{\sigma}_j^+ + \hat{\sigma}_j^-), \quad (\text{S30e})$$

$$\partial_t z_j = \frac{p_{zj}}{M}, \quad (\text{S30f})$$

$$\partial_t x_j = \frac{p_{xj}}{M}, \quad (\text{S30g})$$

where for a generic system operator  $\hat{a}$  we defined  $a \equiv \langle \hat{a} \rangle$ . The effect of temperature enters into the mean field dynamics by sampling the initial position and momentum from a thermal distribution at temperature  $T$ . We consider the cavity to be initially in vacuum  $c(0) = 0$  and the atoms to be in their ground state  $\hat{\sigma}_j^z(0) = -1$  and  $\hat{\sigma}_j^+(0) = 0$ .

We compute the field projection following the same procedure described for the experiment. In Fig. S3, we compare the results of the numerical simulations for the field projection as a function of the pump strength  $\Omega$  with the prediction of the critical pump strength derived in Sec. IIB from a 2D model. We find good agreement between the two methods. The numerical simulation accounts for the internal dynamics of the atoms and for atomic saturation, while the analytical results in Sec. IIB are obtained under the assumption of linear response and adiabaticity of the atomic internal dynamics. The agreement between the analytical prediction and the numerical simulation is thus an *a posteriori* confirmation that our approximated model correctly captures the critical point for atomic self organization.

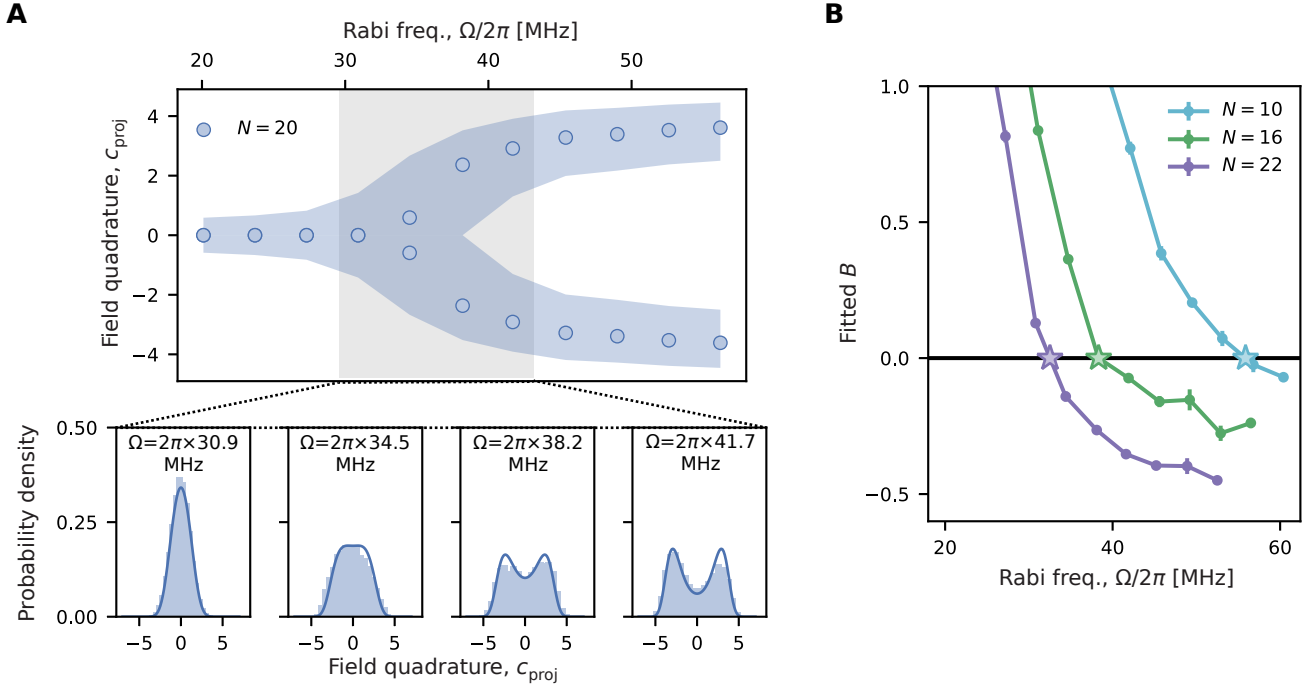


Figure S5. **Interpolation of  $\Omega_c$  from Boltzmann fits.** (A) Data showing the bifurcation for 20 atoms at  $\Delta_{\text{pa}} = 2\pi \times 80$  MHz. Markers represent the maxima of the fitted Boltzmann probability distribution of  $c_{\text{proj}}$ . Blue shaded areas show the width of the distribution at half-maximum. Bottom insets show histograms (light blue) and Boltzmann fits (dark blue) for values of  $\Omega$  in the gray shaded region. (B) By fitting experimentally obtained distributions, such as those shown in (A), to the Boltzmann distribution, we extract the parameter  $B$  at different values of  $\Omega$  for various  $N$ . The  $N$  shown here correspond to the data shown in Fig. 2A of the main text. The value of  $\Omega_c$  (stars) is linearly interpolated from the two points on directly on either side of the  $B = 0$  line. Error bars on the fitted  $B$  values are smaller than the markers. Lines are guides to the eye.

#### D. Dependence of $\Omega_c$ on $\Delta_{\text{pa}}$

Fig. S4 shows how the critical point varies with  $\Delta_{\text{pa}}$ . Because the cavity dispersive shift has a larger effect when the cavity is closer to atomic resonance (see Eq. (S17)), we choose values of  $\Delta_{\text{pc}}$  that approximately compensate for this effect. As a result of this compensation,  $\Delta_{\text{pc}}(T)$  is approximately constant for these data with  $\Delta_{\text{pc}}(T) \simeq -2\pi \times 1.6$  MHz. From the distributions of  $c_{\text{proj}}$  obtained at these parameter settings, we determine the critical points by fitting the data to the Boltzmann distribution (see section E). We see that  $\Omega_c$  displays an approximately linear dependence on  $\Delta_{\text{pa}}$ . By fitting the  $\Omega_c$  data to Equation (4), the 2D analytical prediction, we estimate the atoms' motional temperature to be  $66 \pm 8 \mu\text{K}$ . This is notably higher than our independent temperature measurement would predict [S2]. However, the independent measurement was taken with a pump power far below the critical point, so increased heating from light scattering could contribute to the higher temperature that we now observe.

#### E. Experimental interpolation of the critical point: data and error analysis

As noted in the main text, the critical point is determined by interpolating the value of  $\Omega$  that makes  $B = 0$ , where  $B$  is the coefficient on the quadratic term of the mechanical potential. At each parameter setting, we fit the obtained distributions of  $c_{\text{proj}}$  to the Boltzmann distribution (Equation 5) to extract  $B$ . Examples of such distributions and their Boltzmann fits are shown in Fig. S5A. To estimate the error in this fit of  $B$ , we implement bootstrapping: we randomly draw samples with replacement from the  $c_{\text{proj}}$  distribution at each  $\Omega$  and do the fit again. This is iterated 10 times. The average value and standard deviation of  $B$  is then calculated from the bootstrap samples. The sign of  $B$  determines whether the distribution is unimodal ( $B > 0$ ) or bimodal ( $B < 0$ ), and thus the critical point occurs when  $B = 0$ . As shown in Fig. S5B, the fitted values of  $B$  go from being positive to negative as  $\Omega$  is increased.

Since we lack a complete theoretical model of how  $B$  should vary with  $\Omega$ , we simply linearly interpolate the value of  $\Omega$  that makes  $B = 0$  and use this as  $\Omega_c$ . To do so, we consider the two sampled points directly on either side of  $B = 0$ ; we call them by the coordinates  $(\Omega_1, B_1)$  and  $(\Omega_2, B_2)$ , where  $B_1 > 0$  and  $B_2 < 0$ . Then, our experimental  $\Omega_c$ ,

$\Omega_c^{(\text{exp})}$ , is given by the  $x$ -intercept of the line the passes through these two points:

$$\Omega_c^{(\text{exp})} = \Omega_1 - \frac{B_1(\Omega_1 - \Omega_2)}{B_1 - B_2}. \quad (\text{S31})$$

The standard deviation  $\sigma_{\Omega_c}$  on the critical point is obtained through error propagation:

$$\sigma_{\Omega_c}^2 = \left| \frac{\partial \Omega_c^{(\text{exp})}}{\partial B_1} \right|^2 \sigma_{B_1}^2 + \left| \frac{\partial \Omega_c^{(\text{exp})}}{\partial B_2} \right|^2 \sigma_{B_2}^2 + \left| \frac{\partial \Omega_c^{(\text{exp})}}{\partial \Omega_1} \right|^2 \sigma_{\Omega_1}^2 + \left| \frac{\partial \Omega_c^{(\text{exp})}}{\partial \Omega_2} \right|^2 \sigma_{\Omega_2}^2. \quad (\text{S32})$$

The standard deviations  $\sigma_{B_1}$  and  $\sigma_{B_2}$  are obtained from bootstrapping, while  $\sigma_{\Omega_1}$  and  $\sigma_{\Omega_2}$  are given by an estimate of 10% drift of the pump power over the course of the experimental runs. We note that the linear interpolation is an approximate method for obtaining the critical point, and so the error propagation applied to obtain  $\sigma_{\Omega_c}$  may not accurately reflect the true experimental uncertainty on  $\Omega_c$ .

Our extraction of  $\Omega_c^{(\text{exp})}$  is also subject to systematic errors due to Gaussian noise in our detection and uncertainty in our measurement of the pump Rabi frequency. Gaussian noise, resulting from photon shot noise and electronic detector noise, causes the  $c_{\text{proj}}$  distributions to smear out and thus leads us to systematically overestimate  $\Omega_c^{(\text{exp})}$  when we use the method described above. We theoretically calculate how much the noise affects  $\Omega_c^{(\text{exp})}$  by convoluting a Gaussian distribution, whose width is determined by the fluctuations observed when no atoms are in the cavity, with the Boltzmann distribution. We then perform the same  $B$ -fits and linear interpolation on the convoluted distributions to estimate the percentage by which  $\Omega_c^{(\text{exp})}$  changes. All  $\Omega_c$  data shown in the main text and Fig. S4 have been scaled to account for this systematic error.

The other systematic error we have identified is error in our measurement of  $\Omega$  due to uncertainty in our measurement of the pump beam size at the atoms ( $173 \pm 5 \mu\text{m}$ ), in the positioning of the pump beam relative to the atom array, and in our measurement of the pump power (estimated to be  $\pm 6\%$ ). Since the same beam size and power was applied to all data, these will cause all the  $\Omega_c$  data to be shifted together up to approximately  $\pm 6\%$ . We also note that the average  $\Omega$  seen by the atom array depends on the atom number, since a larger array will see more of the Gaussian profile of the pump beam. To account for this, we average the pump intensity profile over the span of the atom array for each  $N$ , assuming the beam is exactly centered on the array, and factor this into our reported  $\Omega$ ; this systematically shifts  $\Omega$  downwards. It is also possible that the beam is not exactly centered on the atoms; we estimate the uncertainty to be about  $\pm 30 \mu\text{m}$  in both the  $y$  and  $z$  dimensions. This off-centering would reduce  $\Omega$  by up to an additional 6%. As a result, we expect that  $\Omega_c^{(\text{exp})}$  could be systematically shifted upwards by up to 6% or shifted downwards by up to 8.5%, where we have added the downward errors in quadrature.

There are additional systematic error sources whose effects on the critical point have not been quantified. One such source is the tweezer trap frequency being lower at the outer edges of the array due to aberrations in the tweezer optical setup. This should push the critical point lower for larger  $N$ . Similarly, optical aberrations make the tweezer spacing uneven towards the edges of the array; we estimate the deviation to be up to 100 nm along both the cavity and pump axes at the edges of the 22-atom array. We expect this deviation to push the critical point higher for larger atom numbers.

## F. Theoretical calculation of optomechanical susceptibility

We first present an approximate analytical expression for the susceptibility  $\chi$  where we approximate the potential energy of the dominant mode as only containing terms up to fourth order in  $z_{\text{dom}}$ , following Landau's prescription. From now on, we drop the "dom" subscript for convenience of notation. The thermally averaged displacement of the dominant mode is given by

$$\langle z \rangle_{\text{approx}} = \frac{\int_{-\infty}^{+\infty} z \exp\left(-\frac{N}{\sigma^2} \left(\frac{\Omega^2}{6\Omega_c^2} (k^2 z^2 - 3) z^2 + \frac{1}{2} (z - \delta z)^2\right)\right) dz}{\int_{-\infty}^{+\infty} \exp\left(-\frac{N}{\sigma^2} \left(\frac{\Omega^2}{6\Omega_c^2} (k^2 z^2 - 3) z^2 + \frac{1}{2} (z - \delta z)^2\right)\right) dz}. \quad (\text{S33})$$

Here we have defined  $\sigma = \sqrt{\frac{k_B T}{M\nu^2}}$ , which gives the standard deviation of the atomic thermal density distribution in a harmonic tweezer. From this, we obtain an approximation for  $\chi$ :

$$\begin{aligned} \chi_{\text{approx}} &\simeq \left. \frac{\partial \langle z \rangle_{\text{approx}}}{\partial (\delta z)} \right|_{\delta z=0} = \frac{\int_{-\infty}^{+\infty} \frac{Nz^2}{\sigma^2} \exp\left(-\frac{N}{\sigma^2} \left(\frac{\Omega^2}{6\Omega_c^2} (k^2 z^2 - 3)z^2 + \frac{1}{2}z^2\right)\right) dz}{\int_{-\infty}^{+\infty} \exp\left(-\frac{N}{\sigma^2} \left(\frac{\Omega^2}{6\Omega_c^2} (k^2 z^2 - 3)z^2 + \frac{1}{2}z^2\right)\right) dz} \\ &= \frac{\pi(3N(r^2 - 1)I_{-\frac{1}{4}}\left(\frac{3N(r^2-1)^2}{16k^2r^2\sigma^2}\right) - (3N(r^2 - 1)^2 + 8k^2r^2\sigma^2)I_{\frac{1}{4}}\left(\frac{3N(r^2-1)^2}{16k^2r^2\sigma^2}\right) + 3N(r^2 - 1)^2(I_{\frac{3}{4}}\left(\frac{3N(r^2-1)^2}{16k^2r^2\sigma^2}\right) - I_{\frac{5}{4}}\left(\frac{3N(r^2-1)^2}{16k^2r^2\sigma^2}\right))}{4\sqrt{2}k^2r^2(r^2 - 1)\sigma^2 K_{\frac{1}{4}}\left(\frac{3N(r^2-1)^2}{16k^2r^2\sigma^2}\right)}, \end{aligned} \quad (\text{S34})$$

where  $r \equiv \Omega/\Omega_c$  and  $I_\alpha(x)$  and  $K_\alpha(x)$  are modified Bessel functions of the first and second kind respectively.

We can similarly obtain an integral expression for  $\chi$  where we keep the sinusoidal form of the cavity potential. In this case, the average antiphase displacement is

$$\langle z \rangle = \frac{\int_{-\infty}^{+\infty} z \exp\left(-\frac{N}{4k^2\sigma^2} (-r^2 + 2k^2(z - \delta z)^2 + r^2 \cos(2kz))\right) dz}{\int_{-\infty}^{+\infty} \exp\left(-\frac{N}{4k^2\sigma^2} (-r^2 + 2k^2(z - \delta z)^2 + r^2 \cos(2kz))\right) dz}. \quad (\text{S35})$$

Thus, the expression for  $\chi$  becomes

$$\chi \simeq \left. \frac{\partial \langle z \rangle}{\partial (\delta z)} \right|_{\delta z=0} = \frac{\int_{-\infty}^{+\infty} \frac{Nz^2}{\sigma^2} \exp\left(-\frac{N}{4k^2\sigma^2} (-r^2 + 2k^2z^2 + r^2 \cos(2kz))\right) dz}{\int_{-\infty}^{+\infty} \exp\left(-\frac{N}{4k^2\sigma^2} (-r^2 + 2k^2z^2 + r^2 \cos(2kz))\right) dz}. \quad (\text{S36})$$

By numerically computing the integrals in Eq. (S36), we obtain the theory curves shown in Fig. 4C of the main text.

- 
- [S1] M. Endres, H. Bernien, A. Keesling, H. Levine, E. R. Anschuetz, A. Krajenbrink, C. Senko, V. Vuletic, M. Greiner, and M. D. Lukin, Atom-by-atom assembly of defect-free one-dimensional cold atom arrays, *Science* **354**, 1024 (2016).
- [S2] Z. Yan, J. Ho, Y.-H. Lu, S. J. Masson, A. Asenjo-Garcia, and D. M. Stamper-Kurn, Superradiant and Subradiant Cavity Scattering by Atom Arrays, *Physical Review Letters* **131**, 253603 (2023).
- [S3] M. Aspelmeyer, T. J. Kippenberg, and F. Marquardt, Cavity optomechanics, *Rev. Mod. Phys.* **86**, 1391 (2014).
- [S4] V. Vuletić and S. Chu, Laser cooling of atoms, ions, or molecules by coherent scattering, *Phys. Rev. Lett.* **84**, 3787 (2000).
- [S5] V. Vuletić, H. W. Chan, and A. T. Black, Three-dimensional cavity doppler cooling and cavity sideband cooling by coherent scattering, *Phys. Rev. A* **64**, 033405 (2001).
- [S6] P. Domokos and H. Ritsch, Mechanical effects of light in optical resonators, *J. Opt. Soc. Am. B* **20**, 1098 (2003).
- [S7] P. Domokos and H. Ritsch, Collective cooling and self-organization of atoms in a cavity, *Phys. Rev. Lett.* **89**, 253003 (2002).
- [S8] J. K. Asbóth, P. Domokos, H. Ritsch, and A. Vukics, Self-organization of atoms in a cavity field: Threshold, bistability, and scaling laws, *Phys. Rev. A* **72**, 053417 (2005).
- [S9] S. Schütz, S. B. Jäger, and G. Morigi, Thermodynamics and dynamics of atomic self-organization in an optical cavity, *Phys. Rev. A* **92**, 063808 (2015).
- [S10] S. B. Jäger, S. Schütz, and G. Morigi, Mean-field theory of atomic self-organization in optical cavities, *Phys. Rev. A* **94**, 023807 (2016).
- [S11] M. Nairn, L. Giannelli, G. Morigi, S. Slama, B. Olmos, and S. B. Jäger, Spin-self-organization in an optical cavity facilitated by inhomogeneous broadening (2024), arXiv:2407.19706 [cond-mat.quant-gas].
- [S12] M. Le Bellac, F. Mortessagne, and G. G. Batrouni, *Equilibrium and Non-Equilibrium Statistical Thermodynamics* (Cambridge University Press, 2004).
- [S13] When the interatomic separation is an integer (half-integer) multiple of  $\lambda$  the dominant mode is the center-of-mass (antiphase) mode where neighboring atoms move in phase (in phase opposition).